J. Fluid Mech. (2008), *vol.* 611, *pp.* 365–394.
doi:10.1017/S0022112008002899 Printed in the United Kingdom

Trapping of air in impact between a body and shallow water

A. A. KOROBKIN[1]†, A. S. ELLIS[2] AND F. T. SMITH[2]

[1]Lavrentyev Institute of Hydrodynamics, Novosibirsk, 630090, Russia

[2]Dept. of Mathematics, UCL, Gower Street, London WC1E 6BT, UK.

(Received 12 October 2007 and in revised form 18 June 2008)

Near-impact behaviour is investigated for a solid body approaching another solid body with two immiscible incompressible viscous fluids occupying the gap in between. The fluids have viscosity and density ratios which are extreme, the most notable combination being water and air, such that either or both of the bodies are covered by a thin film of water. Air–water interaction and the commonly observed phenomenon of air trapping are of concern in the presence of the two or three thin layers and one or two interfaces. The subcritical regime is of most practical significance here and it leads physically to the effect of inviscid water dynamics coupling with a viscous-dominated air response locally. This physical mechanism induces touchdown (or an approach to touchdown), which is found to occur in the sense that the scaled air-gap thickness shrinks towards zero within a finite scaled time according to analysis performed hand in hand with computation. A global influence on the local touchdown properties is also identified. Comparisons with computations prove favourable. Air trapping is produced between two touchdown positions, at each of which there is a pressure peak; an oblique approach would not affect the finding unless the approach itself is extremely shallow. The mechanism of air–water interaction leading to air trapping is suggested as a quite wide-ranging result.

1. Introduction

The approach of one solid body towards another solid body with liquid between them, and the subsequent squeezing and impact, has diverse applications and interest not only in droplet impact concerned with aircraft or rotorcraft icing (Gent, Dart & Cansdale 2001, Tan & Papadakis 2005, Quero *et al.* 2006) but also in food manufacture, composites manufacture, coating problems, squeeze films, sport-related impacts and meteor cratering. In many cases air or another surrounding medium is also present, yielding possible interactions of at least two fluids in the gap between the bodies. Successive impacts and re-impingements of water droplets combined with air effects in particular have crucial effects on icing of aircraft wings (Purvis & Smith 2004*a*, *b*, 2005*a*, *b*), as seen most recently in the experimental and computational works of Tan & Papadakis (2005) and Quero *et al.* (2006). Our principal concern here is with air and water as the two fluids involved between the two solid bodies.

Trapping of air during and after the impact is a common and important issue in many of the applications; our aim is to enhance its physical understanding. The creation of air pockets leads to significant sound effects, potential damage due to the

† Current address: School of Mathematics, University of East Anglia, Norwich, UK, NR4 7TJ

pressure changes and excessive loads on either of the solid surfaces produced by the water–air combination, uncertainty and possible instability concerning the end result of the whole collision process and/or inconsistency of the required industrial product because of the uneven distribution of one of the fluids involved in manufacture.

The main specific settings implied for study, then, are for a water–air arrangement being squeezed between a lid and a bed and for a rigid body approaching a thin film on a bed, with or without a thin coating of water on the rigid body. See figure 1(*a*, *b*). The investigation here does not apply directly to the scenario of a droplet–air–water-bed configuration of icing interest described above, but the settings are appropriate for modelling the approach to a solid surface of an incident ice lump with or without a water coat. The basic problem of a solid object descending through air onto a water film on a solid bed has been addressed previously for the case of entry into effectively deep water, as in various references above, together with the work of Howison *et al.* (2005) and Purvis & Smith (2005*a*), when air is neglected. Now, however, a new study is required for the case of a relatively shallow film of water in the presence of air. Allowance also needs to be made for a thin coat of water on the incident solid itself, which is now likely to affect the dynamics, whereas such a coat is negligible when the entry is into deep water. The presence of a coat on the incident solid is associated with many applications, including that to sport, as mentioned earlier.

Two-fluid dynamics have been the subject of numerous studies in other contexts. There are comparatively few investigations, however, of the specific air–water or related combinations that are of most concern here, apart from features observed in the experiments by Liow (2001), Thorodssen (2002), in the computational simulations by Josserand & Zaleski (2003), Purvis & Smith (2004*a*), and in other relevant theoretical literature described in Howison, Ockendon & Wilson (1991), Howison, Ockendon & Oliver (2002), Wilson (1991), Korobkin (1997, 1999), Vanden-Broeck & Miloh (1996), Vanden-Broeck (2001), Smith, Li & Wu (2003) and Purvis & Smith (2004*b*), including studies of inviscid or viscous-inviscid waves. Post-impact effects with two-fluid interaction are considered theoretically in Purvis & Smith (2004*b*, 2005*a*). The theoretical findings of Smith *et al.* (2003), in particular, imply two perhaps surprising features holding during the approach of a water droplet to a water film on a solid bed, first that locally the water acts as if inviscid but the air as if viscous, and second that the critical representative Reynolds number, below which the air has such a lubricating action, is typically about 10 million. In the industrial applications above and in many other practical settings, the typical value of the representative Reynolds number is actually less than 100 thousand or not much more, and so the practicability of the subcritical range of Reynolds numbers is highlighted. We also mention here the most recent study of Pan and Law (2007), also concerning the impact of a liquid droplet on to a solid body with a liquid coat. Interestingly, they found that the droplet could merge with or bounce away from the liquid coat, a behaviour which is dependent on the response of the fluid in the gap between the colliding interfaces. There are also fascinating phenomena observed in Protiere, Boudaoud & Couder (2006) and previous related papers associated with the interaction between a liquid drop bouncing on a liquid surface and the interfacial waves excited by the very presence of the drop. This also occurs with several such drops. Finally, the work of Afandizadeh Zargari, Jimack and Walkley (2007) is of related interest here: they study elastohydrodynamic lubrication, in which a lubricant is applied between two contacting surfaces, and they compare and contrast two numerical approaches. Their work demonstrates that large pressures exist in the contact region, but additionally a subsidiary pressure peak described as the Petrusevich spike is seen to exist. An

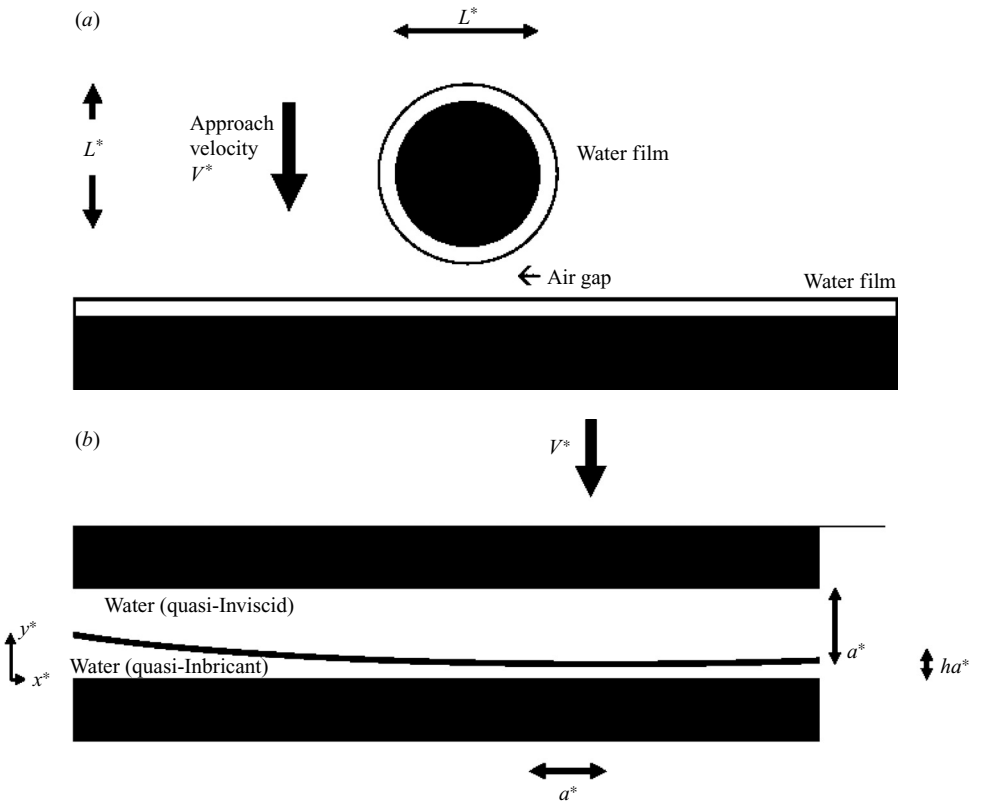

FIGURE 1. (a,b) A solid body (shown shaded) approaches another, with air and one or two thin layers of water in between. The dimensional diagram in (a) has a water–air–water configuration while that in (b) has only one layer of water and gives a more local view; x^*, y^* are Cartesian coordinates. The typical curvatures $1/L^*$ on the global length scale L^* and h^*/a^* on the local scale a^* are comparable so that the small ratios h and a^*/L^* are of similar size. On the local time scale of order ha^*/V^* the water is found to act as if inviscid whereas the air flows as if a lubricant.

apparently similar phenomenon is seen to occur in Smith *et al.* (2003) as well as in the current setting; see § 3.

In Korobkin (1996) a simple two-dimensional problem of a body approaching the interface of two shallow fluids was introduced. Both fluids were treated as inviscid and incompressible. A two-layer shallow-water approximation was used to describe both the fluid motions and the interface deflection. The type of the relevant two-layer shallow-water equations is mixed, and depends on the body shape and its motion. It was found that the maximum of the flow velocity in the gap between the body surface and the fluid interface is the most important parameter, which governs the type of the shallow-water equations: see also Oliver (2002) and the finite-time singularity discussed in the appendix of Purvis and Smith (2004*b*). At the beginning of the process this parameter is small and the equations are of hyperbolic type; during this stage the problem can be solved by the method of characteristics. When the distance between the body and the interface decreases, the parameter increases and the equation type changes from hyperbolic to elliptic, but only locally, where the parameter value exceeds a certain limit. These zones of ellipticity of the shallow-water equations for

two-layer fluid were treated as mixing zones by Korobkin and Khabakhpasheva (1997) (see also Brocchini & Peregrine 1996). The Richardson number Ri, which is inversely proportional to the square of the velocity jump across the interface, was used. The governing equations are of hyperbolic type where $Ri > 1$ and of elliptic type where $Ri < 1$. In the case of an air–water system, the velocity jump is expected to be large when the distance between the air–water interface and the approaching body is small. Also, the mixing of the fluids was modelled approximately: in the zones where $Ri > N$ the shallow-water equations were replaced with the equation $Ri = N$. This means that the governing equations were solved under the constraint $Ri \leqslant N$, where N is a parameter of the problem. It was shown that the extent of the mixing zones grows as the square root of time. In the above simplified analysis the role of viscous effects was not studied.

In Korobkin and Khabakhpasheva (2006) impact onto the boundary of a two-layer compressible fluid was analysed. The penetration depth was much smaller than the layer thicknesses, which is why a complex shock wave pattern was properly reproduced. The layer attached to the boundary can be narrow, as in the case for the air–water system. A thin-layer approximation was suggested by Korobkin (2006) to model the complex characteristics of the liquid surface in the impact region, which accounts for air–water mixing. It is assumed that the impact onto the water surface occurs through a thin layer of air–water mixture on the liquid boundary. This thin layer was modelled as an homogeneous compressible medium with reduced sound speed, while in the main region the liquid was considered as ideal and incompressible. Also in the analysis the aerated layer was assumed to be of small but constant thickness. Nonlinear and viscous effects were not modelled. The predictions by this simplified model were compared with those from Korobkin and Khabakhpasheva (2006) and fairly good agreement was demonstrated.

The combination of air and water involves density and viscosity ratios which are fairly extreme, corresponding to an order of magnitude or two. Direct numerical simulations are difficult to perform accurately for extreme density and viscosity ratios such as those for water with air, but in contrast analysis may then be eased or aided, in the sense that a clear small parameter or two can be inferred. In an attempt to take advantage of that in the present setting we use a small-ratio theory combined with thin-layer properties. One point to emerge from the study by Smith *et al.* (2003) above is that the two-fluid interaction identified there apparently leads to a touchdown (or close approach to touchdown) of the water onto the wall. It is found in the current investigation, involving a rather distinct new physical mechanism, that considerable analytical and numerical evidence can be added to support the view that touchdown is commonly implied in the present two-fluid interactions, which thus appear to produce a physically realistic outcome.

Below, we address the physical setting and the resultant governing equations in § 2, then a computational study in § 3, inferred analytical properties in § 4, and § 5 and finally a discussion in § 6. Two-dimensional laminar unsteady motion is assumed for two incompressible immiscible fluids. For the sake of definiteness the reasoning is couched in terms of a solid object approaching a thin water film on a solid bed and there is a thin film on the incident object too, but the present governing system still remains valid if either of those thin films is absent: see figure 1(a, b). Among other spin-off applications the system obtained also models elastic-layer effects on a thin film. The system in the two-fluid interaction of present concern, which depends physically on lubrication forces in the air coupled with unsteady potential-flow dynamics in the water, controls the evolution of the air gap thickness and the induced surface pressure.

2. Physical setting and governing equations

The broad physical setting and the full system of equations and boundary conditions are given in § 2.1. Following that, § 2.2 presents the physical arguments based on the rather extreme values of the density ratio for the two fluids involved in the impacting process which lead, in § 2.3, to a reduction of the system to a coupled pair of nonlinear partial differential equations.

2.1. *The physical setting and the full governing system*

We consider a water-coated rigid body approaching a quasi-flat fixed solid surface on which there is a thin layer or film of surface water initially at rest. The direction of approach is normal to the solid surface, i.e. in the negative y^* direction, and air which is also initially at rest occupies the gap between the two regions of water, as demonstrated in figure 1(a,b). An asterisk denotes a dimensional quantity. The well-known phenomenon of air trapping is of prime interest. The aim of the study is to investigate a possibly significant role being played by air–water interaction within relatively short length scales in trapping air in pockets, over a relatively short time scale typically, and to investigate also whether such interaction and consequent trapping are common occurrences. In fact the study finds that they are very common indeed. The subsequent theory is taken as two-dimensional in the x-y plane, although it also applies in axisymmetric settings as discussed in § 6. Strictly, the water and air should be referred to as fluids 1, 2 respectively, since the theory to be developed in the next subsection is based on two such fluids having vanishingly small density and viscosity ratios.

For each fluid the continuity equation is

$$\nabla \cdot \boldsymbol{u} = 0, \tag{2.1a}$$

with an assumption of incompressibility which is justified later on, while in the two regions of water the Navier–Stokes equations take the form

$$(\partial_t + \boldsymbol{u} \cdot \nabla)\boldsymbol{u} = -\nabla p + Re_1^{-1}\nabla^2 \boldsymbol{u}, \tag{2.1b}$$

and in the air we have

$$(\partial_t + \boldsymbol{u} \cdot \nabla)\boldsymbol{u} = -(\rho_1/\rho_2)\nabla p + Re_1^{-1}(\nu_2/\nu_1)\nabla^2 \boldsymbol{u}. \tag{2.1c}$$

The equations above are written in non-dimensional terms. The velocity vector $\boldsymbol{u} = (u, v)$, the corresponding Cartesian coordinates (x, y), the pressure p and the time t have been non-dimensionalized based on the rigid-body approach speed V^*, a representative length scale L^*, $\rho_1^* V^{*2}$ and L^*/V^* respectively. In particular $(x^*, y^*) = L^*(x, y)$. The length L^* is a global quantity such as the rigid-body diameter if the rigid body is of circular shape as in figure 1(a), while ρ_1^*, ρ_2^* are the densities of the water and air respectively, $\mu_1^* (= \rho_1^* \nu_1^*)$, $\mu_2^* (= \rho_2^* \nu_2^*)$ are their respective viscosities and ν_1^*, ν_2^* are their respective kinematic viscosities. The coordinates used are centred for convenience in the impact area, such that in the water–air–water configuration of figure 1(a) the origin lies directly below the cylinder on the original surface of undisturbed water, whereas in figure 1(b), which has only one water and one air layer, the origin lies on the lower solid surface. The pressure is measured relative to the atmospheric value for the air. Also $Re_1 = V^* L^*/\nu_1^*$ is the water-based Reynolds number, the vector ∇ denotes the operator (∂_x, ∂_y), and gravity, surface tension and compressibility are neglected: compare with the Appendix. The appropriate boundary conditions in general are the well-known ones of prescribed velocities on the solid

surfaces and continuity of the velocities and stress components (along with the kinematic conditions) at the fluid–fluid interfaces. We shall focus below mostly on the water–air–water configuration of figure 1(*a*), in which the two interfaces, namely the interface between the water coating and the air gap and that between the air gap and the surface water layer, are unknown in advance, as are the induced surface pressures.

When the approaching body and the solid surface are still sufficiently far apart, there is virtually no interaction between them or between the water layers on them, as the air in the gap acts almost as a void. In practice it is a common experience that substantial interaction by means of feedback between the water and air flow dynamics usually begins only when impact is neared. On the verge of impact, the aspect ratio h of the layer of air can thus be assumed small. Moreover, the present setting of an impact has local interaction which is rapid (see the time scale below) and involves the relatively thin layer of air between the coating of water and the thin water layer on the solid surface. The reason for such small-scale or rapid occurrences lies in the small ratios of density and viscosity for air and water, a feature that is to be exploited in the theory here. This leads to the investigation below.

2.2. *Physical reasoning for reduced governing equations*

The nature of the flow solution on the verge of impact follows from an order-of-magnitude argument, given that the length scales in the water are short near impact, such that $(x, y) = (X, Y)a^*/L^*$ where the characteristic dimensional local length $a^* \ll L^*$, whereas the layer of air which lies along or near the x-axis has length scales given by $(x, y) = (X, hy_2)a^*/L^*$. Here the ratio a^*/L^* is comparable with h for a smooth rigid-body shape of finite curvature. The typical time scale $t = h^2T$ must also be short such that $T \sim 1$ because of the $O(1)$ approach speed and the h^2 size of the non-dimensional thickness of the air layer. In consequence, the water in both the coating and the surface layer experiences a normal velocity v of order unity, because of the definition of the normal approach speed of -1 combined with the kinematic boundary conditions at the two interfaces, and together with this the water can be expected to experience a tangential velocity u of order unity through the continuity equation. Hence the pressure response p within the water is typically of size h^{-1}, from the balance of the representative pressure gradient $\partial p/\partial x$ with the acceleration effect $\partial u/\partial t$ of size h^{-2}, which overwhelms all the $(O(h^{-1}))$ inertial effects such as $u\partial u/\partial X$ due to the active t and x scales. The reasoning here in both regions of water takes viscous forces to be negligible, an assumption which is tested later. Meanwhile, within the air the normal velocity v must again be of order unity in view of the kinematic condition, forcing u to be of size h^{-1} because of the continuity balance, while the pressure p has to be of order h^{-1} through the normal stress condition across the two interfaces, which in essence requires continuity of pressure there as verified in the Appendix. The form of the flow solutions is therefore inferred as

$$(u, v, p) = (u_1, v_1, h^{-1}p_1) + \cdots \text{in water regions}, \tag{2.2a}$$

$$(u, v, p) = (h^{-1}u_2, v_2, h^{-1}p_2) + \cdots \text{in the air gap}. \tag{2.2b}$$

These asymptotic expansions for the velocities and pressure in the two fluids are then substituted into (2.1*a–c*).

The theory also crucially takes the density and viscosity ratios ρ_2^*/ρ_1^* and μ_2^*/μ_1^* of the air and water to be small and, for convenience, comparable such that the ratio ν_2^*/ν_1^* can be considered as of order unity; we should mention that representative

values of the density and viscosity ratios are 1/828 to 1/772 and 1/55 to 1/100 in turn within the temperature range 0–20°C approximately. The dominant equations of motion in the water coating and in the surface water layer as verified by equations (A39) and (A42) of the Appendix are therefore

$$\partial u_1/\partial X + \partial v_1/\partial Y = 0, \tag{2.3a}$$

$$\partial u_1/\partial T = -\partial p_1/\partial X, \tag{2.3b}$$

$$\partial v_1/\partial T = -\partial p_1/\partial Y, \tag{2.3c}$$

from (2.1*a*, *b*), whereas in the air gap the resulting balances are from (2.1*a*, *c*), which give

$$\partial u_2/\partial X + \partial v_2/\partial y_2 = 0, \tag{2.4a}$$

$$0 = -h^{-2}(\rho_1^*/\rho_2^*)\partial p_2/\partial X + h^{-5}Re_1^{-1}(\nu_2^*/\nu_1^*)\partial^2 u_2/\partial y_2^2, \tag{2.4b}$$

$$0 = -(\rho_1^*/\rho_2^*)\partial p_2/\partial y_2. \tag{2.4c}$$

The main governing equations in the water are thus those of unsteady potential flow, while those in the air gap are of a lubricating thin layer.

Concerning boundary conditions as well as the validity of the approximations used, matching at the two unknown interfaces defined as $y_2 = F^+(X, T)$ and $F^-(X, T)$, say, requires, among other conditions, the water pressures $p_1(X, Y = 0+, T)$, $p_1(X, Y = 0-, T)$ to be equal to the air gap pressure $p_2(X, T)$, which is independent of y_2 from (2.4*c*), is also unknown and will be denoted by $P(X, T)$. Here, for the water flows the viscous effects are negligible provided simply that the global Reynolds number Re_1 is large, and the inertial effects are negligible by virtue of the reasoning shown earlier in the paragraph. For the air the typical ratio of the two dominant terms in the x-momentum equation (2.4*b*) can be written as $\Gamma = \mu_2^*/(h^3\rho_1^* V^* L^*)$ which is assumed to be of order unity, while the acceleration and inertial effects are comparatively small provided h is large relative to the density ratio ρ_2^*/ρ_1^*; h must also be small relative to ρ_1^*/ρ_2^* and $(\mu_2^*/\mu_1^*)^{1/3}$. Further, Γ being of order unity means that the global Reynolds number Re_1 is comparable with the ratio $\mu_2^*/(\mu_1^* h^3)$. The theory therefore holds for values of the global Reynolds number Re_1 that are large but less than approximately $(\rho_1^{*2}\nu_2^*)/(\rho_2^{*2}\nu_1^*)$, giving a critical value of Re_1 of more than 10 million for the air–water combination as mentioned in the Introduction and as Smith *et al.* (2003) found. The Appendix provides more discussion and detailed background concerning the parameters, the validity of the governing equations, the boundary conditions, the effects of compressibility and the viscous or inviscid influences in two- or three-dimensional settings. Furthermore, surface tension effects are neglected here since they can be taken to be mostly minor in the present configurations, where the representative Weber numbers are quite large, of the order of 10^4 or more. The effects were addressed in the current type of configuration by Purvis & Smith (2004*b*), who noted that a major influence only appears in the presence of extreme interfacial curvatures, for example. In the current setting, such curvatures are found to occur only at the approach to touchdown, which is described later and which is bound to bring in extra physical effects such as surface tension, non-slenderness or increased nonlinear interaction, of course.

2.3. *The reduced equations*

The induced water pressure p_1 satisfies Laplace's equation from (2.3*a–c*), subject to the interfacial conditions that $p_1 \to P(X, T)$ and $\partial p_1/\partial Y \to -\partial^2 F^+(X, T)/\partial T^2$ or $-\partial^2 F^-(X, T)/\partial T^2$ as $Y \to 0+$ or $0-$, the effective normal velocity conditions

$\partial p_1/\partial Y = 0$ at $Y = -H$ and at $Y = HS(X,T)$ because of the solid surfaces there combined with the uniform approach velocity, and boundedness in the far field at large positive or negative X. Here H is the scaled depth of the original surface layer, whereas $HS(X,T)$ denotes the scaled shape of the incident rigid body relative to the air gap position where Y is small. If either of H, HS is large we obtain a Cauchy–Hilbert integral relation between P, $F^+(X,T) - F^-(X,T)$ as in Smith *et al.* (2003), corresponding to a droplet–air–solid interaction, for instance. This is as might be expected, since a relatively thin layer has a negligible effect compared with the larger one in general. Our interest is more in the case of H, HS both being small, in which case thin-layer behaviour holds in the two water regions and the flow solution then yields the relation

$$\alpha_1 P_{XX} = -F_{TT} \tag{2.5}$$

between the surface pressure $P(X,T)$ and the gap shape effect $F(X,T)$, where $\alpha_1 = H(S+1)$ while $F = (F^+ - F^-)$ is the scaled gap width. It is clear that the interaction law (2.5) holds whether there is a water coat present (non-zero S) or not (zero S) on the upper solid, and likewise on the lower solid.

In the air gap, on the other hand, the lubrication properties (2.4*a–c*) and the interfacial conditions lead to the Reynolds lubrication equation coupling the unknown scaled pressure $P(X,T)$ and gap shape $F(X,T)$ in the form

$$(F^3 P_X)_X = \alpha_2 F_T, \tag{2.6}$$

where the positive constant $\alpha_2 = 12\Gamma$. The scaled pressure P inside the air and water regions must tend to zero at large positive or negative X in view of the general atmospheric pressure. Also, a convenient normalized condition can be applied to the gap shape in the far field, and to the shape at early times, such that

$$F \sim X^2 - T,\ P \to 0 \text{ as } |X| \to \infty \text{ or as } T \to -\infty, \tag{2.7}$$

which applies strictly for an incident locally parabolic shape of the interface, when or where interaction is still weak, and is in line with $v \to -1$ in the incoming motion.

Solution properties of the coupled equations (2.5), (2.6) for F, P are addressed in the next sections. It is worth remarking here that the pressure-shape law (2.5) acts in some sense as a surrogate for the previous Cauchy–Hilbert law of Smith *et al.* (2003) noted earlier, just as in external aerodynamic and internal flow pressure-displacement laws involving interacting boundary layers: see, for example, Smith (1982) and Sobey (2000). In addition, however, the present law (2.5) allows considerably more, and clearer, numerical and analytical progress to be made than in the previous regime, as well as enlarging the range of application.

3. Computational solutions

Computational solutions were sought by adapting the numerical method of Smith *et al.* (2003) used for the Cauchy–Hilbert case, based on compact differencing of fourth-order spatial accuracy with the temporal treatment having second-order accuracy. The adaptation involved discretizing (2.5) in the form (3.1) below.

The unknown functions F_T, P_X, P_{XX}, F_X are written as q, r, s, E respectively, so that (2.5), (2.6) can be discretized consistently as the nonlinear system

$$\left(q_i^{(m+1)} - q_i^{(m)}\right)/DT = -s_i, \tag{3.1}$$

$$F_i^3 s_i + 3F_i^2 E_i r_i = \alpha_2 q_i, \tag{3.2}$$

with α_1 being normalized to unity here and α_2 to 12 without loss of generality. The system (3.1), (3.2) holds at each $X = X_i$ station, DT is the time step, and time-averaged functions are calculated in the method. The scripts denote the discrete solutions at successive time levels. The relations between the local values of q, r, s, E and those of F, P inferred from the definitions above are treated as in equations (5.3)–(5.7d) of Smith *et al.* (2003), and then a global iteration is applied at each time level. Appropriate grids were found to be with typical steps of 0.01 in X between -20 and 20 and a typical time step of 0.00002, depending on the circumstances, and the grid effects on the solutions are then found to be very small as in earlier work. Initial conditions are set at a suitably large negative time.

The method is found to work considerably faster with the current local relation (2.5) than in the Cauchy–Hilbert case, as is perhaps to be expected.

The results are presented in figure 2(*a–d*). The flow solution starts at relatively large negative scaled time when the solid surfaces are well apart and there is little interaction or feedback via the air. The feedback then gradually comes into play. Figures 2(*a*) and 2(*b*) show the solutions for the scaled gap width F, with the latter providing a closer view, and figure 2(*c*) shows the scaled surface pressure P, and we should remark here that, throughout, the flow remains symmetric about the original symmetry line $X = 0$. Figure 2(*d*) shows the minimum value $F_{\min}$ of the scaled shape F at a given time and the corresponding X value $X_{\min}$ at which the minimum is located. In figure 2(*a–d*) the calculation was run from a starting time T of -16, and results in figure 2(*a–c*) are plotted for times T of -3.90 and beyond. In particular, figure 2(*a*) gives F versus X at time intervals of 0.1; figure 2(*b*) then provides a closer view of F with time intervals of 0.1 for T less than 1.0 and interval 0.025 for subsequent times up to 1.625, by which stage $F_{\min}$ is clearly becoming very small; and figure 2(*c*) has the pressure response P plotted against X for the same intervals as in 2(*b*), except that the interval is reduced to 0.0025 for T between 1.60 and 1.645 to highlight the behaviour near the end of the calculation including a slight localized pressure peak: see the discussion of touchdown later. Concerning figure 2(*d*), the location of $X_{\min}$ remains at zero until T is approximately -1.55, after which $X_{\min}$ increases monotonically. Actually there are then two such locations by the virtue of symmetry about $X = 0$, but we present only the location to the right of the symmetry position. Also shown as a dashed curve in the same subfigure, for the purposes of comparison and checking on accuracy, is an analytical solution for the symmetry plane value of F, which is described in the next section and which holds for all time, corresponding to $F_{\min}$ for the times prior to about -1.55 when $X_{\min}$ is zero. The analytical result is found to agree very closely indeed with the present computational solutions as indicated. The interface shape F is concave upwards everywhere at early times in the calculation, in keeping with the initial condition, which is in essence as in (2.7), but eventually the shape near the symmetry axis becomes convex upwards and the descent of F in the centre at the symmetry axis is slowed. These changes are due to the air-cushioning effect via the nonlinear interaction present in (2.5)–(2.7), and the changes gradually spread outwards from the symmetry axis. Along with this there is a continuing reduction as time proceeds in the minimum value of F encountered at an off-centre location (actually two such locations, by symmetry) and a gradual but increasing appearance of two slight pressure peaks again away from the symmetry station.

The numerical solutions just described appear to point quite clearly to touchdown occurring, in the sense that F appears to tend to zero, within a finite scaled time. A

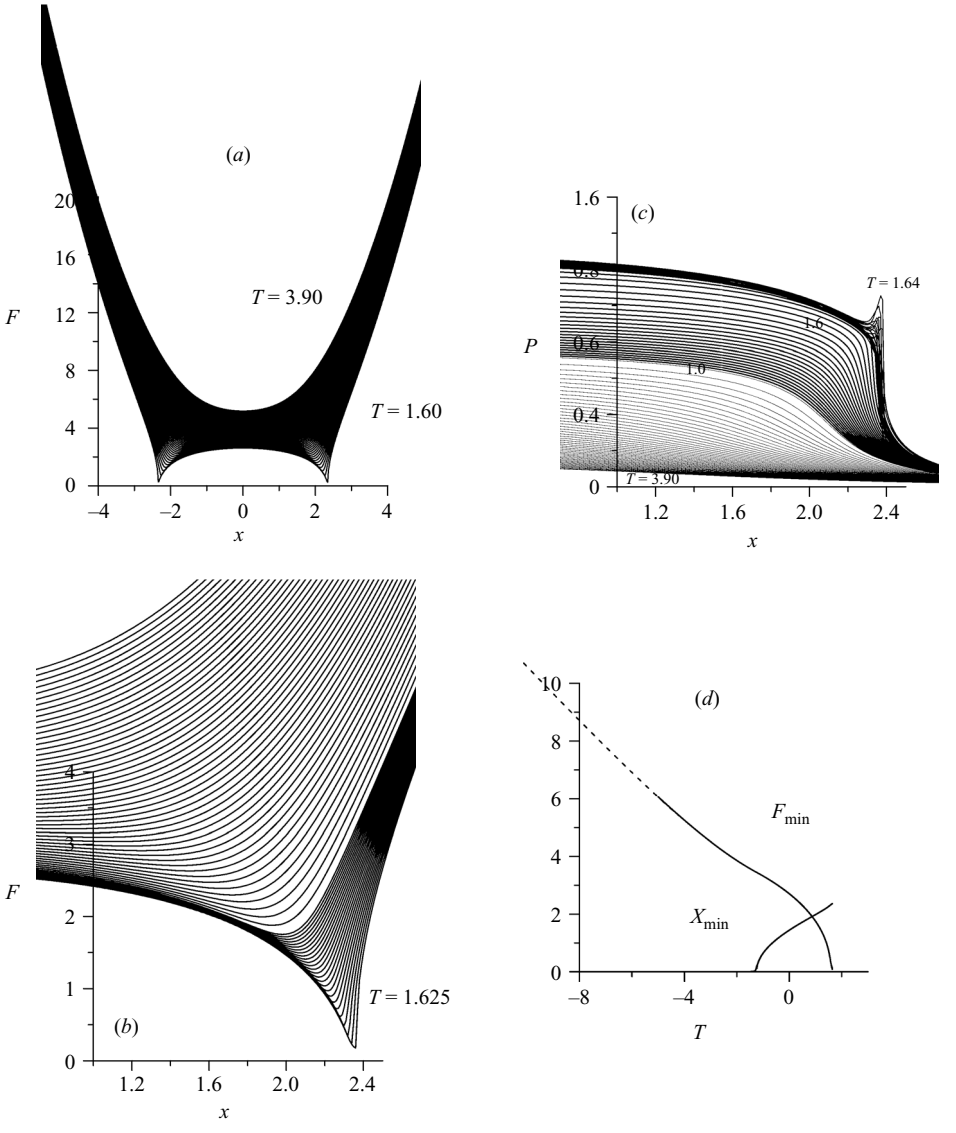

FIGURE 2. Evolution of scaled gap width shape F (a), with close-up (b), and scaled surface pressure distribution P (c). (d) The minimum gap height $F_{\min}$ and corresponding location $X_{\min}$, versus time T, together with a comparison with the analytical result (dashed) from § 4 which holds for $F_{\min}$ while $X_{\min}$ is zero.

loose approximation in which the left-hand side of (2.6) is replaced by $F^3\partial^2 P/\partial X^2$ supports the trend to touchdown, in the sense that (2.5), (2.6) then combine to give $\partial^2 F/\partial T^2 = -\alpha_1\alpha_2(\partial F/\partial T)/F^3$ in effect. This differential equation allows $F \propto (T_0 - T)^{1/3}$, which points to a touchdown event occurring at time T_0 say, and which also confirms the important role of the flexibility of the unknown interface shape in producing such an event. The implied touchdown, or close approach to touchdown, is double-pronged, being off-centre rather than on the symmetry axis, and so it acts to trap air between the two touchdown points.

4. Analytical properties

4.1. *Close to the symmetry line*

The pressure-shape outer relation of current interest is comparatively simple and local, given by (2.5), and this allows very useful progress to be made through an investigation of the flow behaviour near the symmetry line. Such an investigation yields nothing useful in the case of Smith *et al.* (2003), by the way, because of the non-local nature of the different outer pressure-shape relation holding in their case. In our case, the flow solution close to the symmetry line or plane $X = 0$ expands for sufficiently small X as

$$F(X,T) = F_0(T) + F_2(T)X^2 + \cdots, \quad P(X,T) = P_0(T) + P_2(T)X^2 + \cdots, \quad (4.1a,b)$$

where from substitution into (2.5), (2.6) the unknown shape and pressure coefficients as functions of time T are controlled by

$$2P_2 = -F_0'', \quad 2\alpha P_2 F_0^3 = F_0', \quad (4.2a,b)$$

$$12P_4 = -F_2'', \quad 3\alpha\{6P_2F_0^2F_2 + 4P_4F_0^3\} = F_2', \quad (4.3a,b)$$

and so on, with the positive constant α denoting $1/\alpha_2$ and each prime denoting differentiation with respect to T. The pressure term P_0 remains undetermined by this local analysis, as might be expected since the far-field condition in (2.7) has to be satisfied. Combining (4.2a,b) yields a nonlinear ordinary differential equation for the thickness at the symmetry line, namely

$$\alpha F_0^3 F_0'' + F_0' = 0, \quad (4.4)$$

which is subject to the initial behaviour

$$F_0(T) \sim -T - \hat{a}^2/T - \cdots \text{ as } T \to -\infty \quad (4.5)$$

in view of (2.7), with $2\hat{a}^2\alpha = 1$ defining $\hat{a}$, which is positive. The solution for F_0 and hence P_2 has the parametric form

$$F_0 = \hat{a}\sigma, \quad P_2 = (1-\sigma^2)/(\hat{a}\sigma^5), \quad T = \hat{a}\left\{-\sigma + \frac{1}{2}\ln((\sigma+1)/(\sigma-1))\right\}. \quad (4.6)$$

Here F_0 is shown in figure 3(a), whereas the pressure term P_2 is in figure 3(d). It is significant that the present local solution persists for all scaled time and $F_0 > \hat{a}$ throughout, which implies in particular that touchdown cannot occur at the symmetry plane, while the pressure is always maximal at the symmetry plane and its second derivative P_2 decays like T^{-3} at large positive scaled time.

The second-order solution stemming from (4.3a,b) determines the gap curvature and the pressure correction, which are also sought conveniently in terms of σ rather than T directly and are found to have the form

$$F_2 = 1 + \sum_{(1,\infty)} c_k\sigma^{-2k}, \quad P_4 = (\sigma^2-1)/(6\hat{a}^2\sigma^6)\sum_{(0,\infty)}(2k+9)c_k\sigma^{-2k}, \quad (4.7a,b)$$

where

$$c_0 = 1, \quad c_1 = -3, \quad c_{k+1} = c_k\{1 - 2/(k+1) - 6/((k+1)(2k+3))\} \text{ for } k > 0. \quad (4.7c)$$

Similarly, at the next order we obtain the shape and pressure contributions

$$F_4 = (10/\hat{a})\sum_{(0,\infty)} S_m\sigma^{-2m-1}, \quad P_6 = (\sigma^2-1)/(3\hat{a}^3\sigma^6)\sum_{(0,\infty)}(4(m+8)S_m + D_m)\sigma^{-2m-1}, \quad (4.8a,b)$$

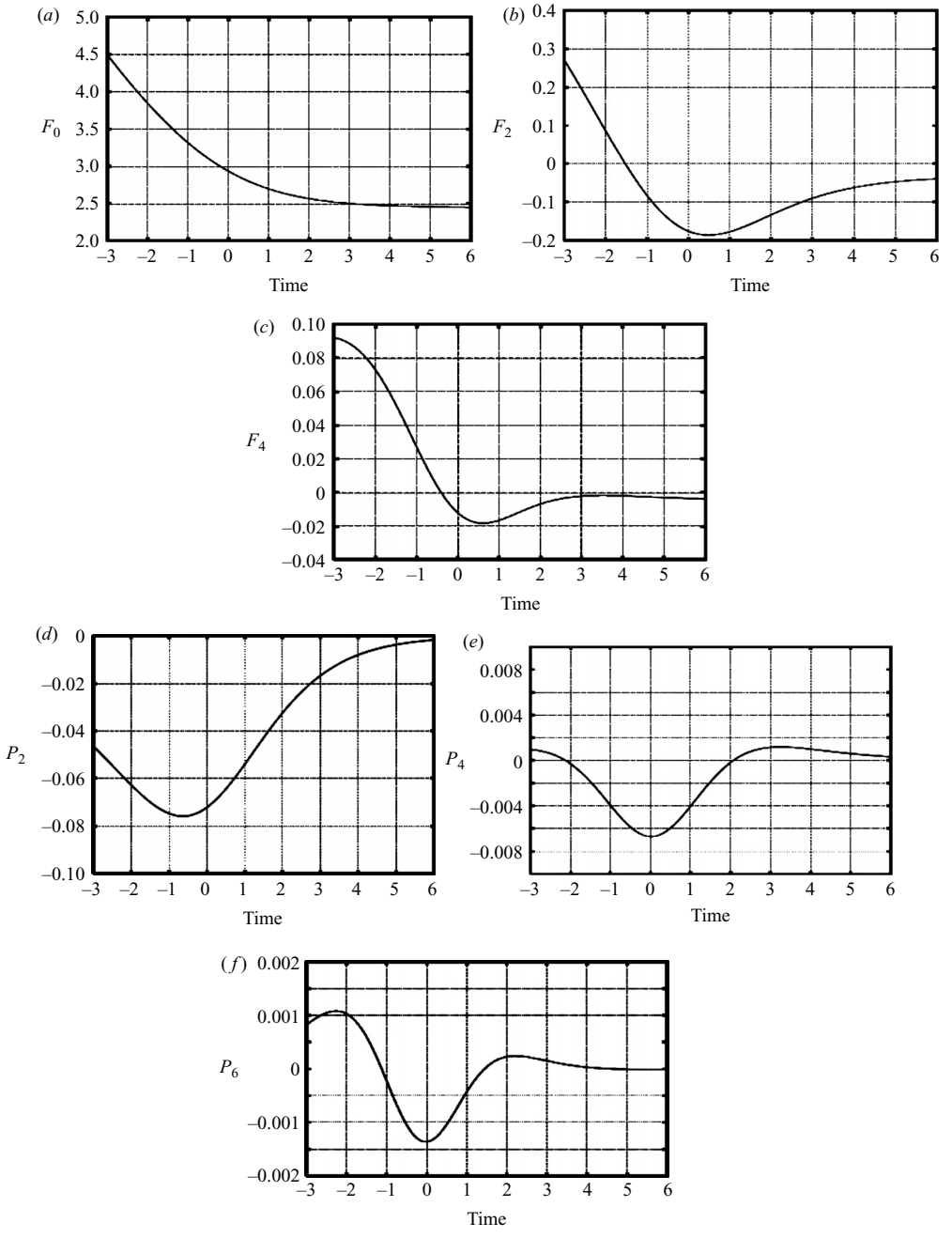

FIGURE 3. The contributions (*a–c*) F_0, F_2, F_4 and P_2, P_4, P_6 (*d–f*), plotted against scaled time.

in which

$$D_m = -2\sum_{(0,m)}(m-k+3)c_k c_{m-k}, \quad (2m+3)(2m+4)S_{m+1} = (4m^2+6m-28)S_m - D_m \quad (4.8c)$$

for non-negative m, with S_0 being zero. These higher-order results are also presented in figure 3(*b,c,e,f*). It is seen from $F_2(T)$ that initially the curvature of the air gap is

positive, but this changes sign to negative at a time T of -1.55. Again, all the pressure terms $P_k(T)$, for $k = 2$ and above, tend to zero with increasing time, giving a trend which suggests that the pressure near the symmetry plane becomes uniform; this, when taken together with the computations described earlier and with the subsequent analysis, can be interpreted as trapping air with the formation of a cavity, in effect.

4.2. *The wider implication*

An inference about the whole flow solution can also be drawn from the above spatial symmetry arguments. Taking the derivative of equation (2.6) in time, then putting $c = F^3 q$ with $q = P_X$ and coupling this with (2.5), yields the balance $\partial[\alpha \partial c/\partial T + q]/\partial X = 0$. The symmetry features above, however, show that both q, c are zero at the station $X = 0$. Hence integration with respect to X gives the explicit result $\alpha \partial c/\partial T + q = 0$, which implies that

$$\alpha F^3 c_T + c = 0. \tag{4.9}$$

Simultaneously, (2.6) now becomes

$$\alpha c_X = F_T. \tag{4.10}$$

The equations (4.9), (4.10) form a coupled system governing the evolution of $F(X, T)$, $c(X, T)$, which in a strong sense are an integration of the previously studied system (2.5), (2.6) as can be observed in the total number of temporal derivatives involved, and these new equations not only apply for all stations X but also prove helpful in the consideration of touchdown. Indeed, the feature inferred from the symmetry plane analysis that the effective constant of integration on the right-hand side of (4.9) must be zero proves crucial in tying down the touchdown properties in the next section. The solution remains physically valid provided that F remains positive.

Overall, the present section has shown that useful information can be gleaned from the flow response near the symmetry line. In particular, the air gap always remains open, in the sence that F remains positive, lying above the value $(2\alpha)^{-1/2}$, and so touchdown cannot occur there and must be located elsewhere if it occurs at all. The symmetry-line properties also provide a check on the numerical work of the preceding section.

5. Touchdown

The possibility of touchdown in which the scaled gap thickness F tends to zero is now examined. This has to be at a station $X = X_0$, say, other than a symmetry one, which is described in the previous section, and the touchdown is envisaged as occurring at some finite time $T \to T_0-$, say. It should be re-emphasized straight away that, strictly, only an approach to touchdown is addressed here, not a full closure of the air gap. The approach involves, in effect, a positive spike in the local pressure as in figure 2. On each side of the spike the curvature of the pressure plot is positive, which corresponds to a deceleration in the closing of the gap in view of the inviscid relation (2.5), although the interfacial velocity locally is negative on one side of the spike and positive on the other to preserve the balance in the viscous requirement (2.6). In the middle of the spike the pressure curvature necessarily reverses sign and that is where the gap closure is accelerated towards touchdown. (The novelty in terms of the touchdown here compared with the Smith *et al.* (2003) case lies in the much simpler outer relation between pressure and shape, which is a local relation as opposed to the non-local one in their case.)

An exact solution holds in principle here, having a similarity form with $(X - X_0)/(T_0 - T)^m = \xi$ being of $O(1)$ as $T \to T_0-$, the power m being expected to be positive, and

$$F(X,T) = (T_0 - T)^n f(\xi), \quad c(X,T) = (T_0 - T)^\theta D(\xi), \tag{5.1}$$

where the power n is positive to ensure that F tends to zero and the function $f(\xi)$ is also positive. The present region of interest has ξ running from minus infinity to plus infinity. Substitution into (4.9), (4.10) immediately leads to a balance, requiring the powers to satisfy $n = 1/3, \theta = m - 2/3$, and produces the interacting pair of nonlinear ordinary differential equations

$$\alpha f^3(-\theta D + m\xi D_\xi) + D = 0, \quad \alpha D_\xi = -\tfrac{1}{3} f + m\xi f_\xi \tag{5.2a,b}$$

for the unknown functions f, D.

Now, although (5.2a) evaluated at ξ zero suggests two options, that either $\alpha\theta f(0)^3 = 1$ or $D(0)$ is zero, the latter of these can be discounted because it eventually points to $f(0)$ being negative. Consequently $f(0) = (\alpha\theta)^{-1/3}$, while $D(0)$ must be non-zero and the restriction $\theta > 0$ holds, implying that $m > 2/3$. We therefore put

$$f = (\alpha\theta)^{-1/3} M, \quad D = |D(0)| N, \quad \xi = E\eta \tag{5.3}$$

which, with E chosen as $\alpha|D(0)|(\alpha\theta)^{1/3}/m$ for convenience, transforms (5.2a,b) into the coupled pair

$$N' = N(M^3 - 1)/(\gamma\eta M^3), \quad M' = (N' + \beta M)/\eta \tag{5.4a,b}$$

for $M(\eta), N(\eta)$, with the prime now standing for $\mathrm{d}/\mathrm{d}\eta$. Here the constants are $\beta = 1/(3m)$, and $\gamma = m/(m - 2/3)$, and both are positive. The nonlinear pair (5.4a,b) is to be solved for $-\infty < \eta < \infty$ nominally and subject to the conditions

$$M(0) = 1, \quad N(0) = -1 \tag{5.4c,d}$$

without loss of generality: we have in mind here the right-hand touchdown indicated by figure 2, whereas the alternative of $N(0)$ being $+1$, which corresponds to a sign change in both N, η, leaving (5.4a,b) unaltered, corresponds to the implied left-hand touchdown. Moreover, the local behaviour near the sensitive position of η zero is noted here,

$$M(\eta) = 1 + \tfrac{1}{3}\beta\gamma\eta + O(\eta^2), \quad N(\eta) = -1 - \beta\eta + \beta\gamma(1 - \beta)\eta^2/6 + O(\eta^3), \tag{5.5a,b}$$

which at first sight appears suitable for a numerical marching scheme for positive or negative η, while the relative far field is expected to have

$$M(\eta) \propto |\eta|^\beta, \quad N(\eta) \propto |\eta|^{1/\gamma} \text{ as } |\eta| \to \infty \tag{5.6a,b}$$

from (5.4a,b). The far-field trends suggested in (5.6a,b) match the touchdown solution as required, with the temporally regular behaviour in the bulk of the flow outside the touchdown region.

Numerical experiments, however, which tackled (5.4a)–(5.5b) by shooting backwards in η by means of a Runge–Kutta scheme, revealed, or at least suggested, that the solution exhibits local branching behaviour near $\eta = 0$, and is very sensitive to the starting point at small η. Many such solutions in fact continued backwards in η and led on satisfactorily to the asymptotic form (5.6a,b) at large negative η (whereas other solutions terminate in a singularity at a finite negative value of η, which will concern us later), but the presence of branching cast doubt on their validity. Analytically the

system is found to possess an eigenfunction, as follows. For small negative η the expansions (5.5a,b) can be supplemented in the form

$$M(\eta) = 1 - \cdots + A\mathrm{e}^{+3/(\gamma\eta)} + \cdots, \quad N(\eta) = -1 - \cdots + A\eta\mathrm{e}^{+3/(\gamma\eta)} + \cdots, \qquad (5.7a,b)$$

including exponentially small terms as shown, which are consistent with the governing equations (5.4a,b), but the constant coefficient A is undetermined locally. This eigenfunction involving an unknown multiplicative coefficient explains the branching in the numerical shooting study for $\eta < 0$, and indeed means that a shooting method there is hindered. Moreover, after noticing that the eigenfunction cannot be present in $\eta > 0$ simply because the function involved is exponentially large rather than small, and after investigating shorter length scales much closer to X_0, we conclude that the coefficient A must be zero on physical grounds, since there is no separate physical source closer to X_0. Thus, only integer powers of η are permissible in the complete series expansion implied by (5.5a,b).

A linearized solution holding at large values of m is found to confirm the eigenvalue above and also shows that there is a smooth solution for all η then.

The form we require, however, is expected to be for $m = 1$ in view of the relative effects at large positive or negative η and matching with the remainder of the flow solution away from the touchdown station (s), at the finite touchdown time. In that case there is an exact solution of (5.4a,b), namely

$$M = \hat{L}^{-1}(\eta + \hat{L}^3)^{1/3}, \quad N = -\hat{L}^3 M, \quad \text{for } \eta > \eta_0, \qquad (5.8a)$$

$$M = N = 0 \quad \text{for } \eta < \eta_0, \qquad (5.8b)$$

where $\eta_0 = -\hat{L}^3$ and $\hat{L}$ is a positive constant; the normalization in (5.4c,d) sets $\hat{L}$ equal to unity. The form (5.8a,b) also satisfies (5.6a,b) formally, as well as the requirement that the coefficient A in (5.7a,b) must be zero.

There must of course be a smoothing zone between the double exact behaviours in (5.8a,b). In fact, close to $\eta = \eta_0$ the expansions

$$F(X,T) = (T_o - T)^{\tilde{q}}\tilde{f}(\tilde{\xi}) + \cdots, \quad c(X,T) = (T_0 - T)^{\tilde{r}}\tilde{c}(\tilde{\xi}) + \cdots \qquad (5.9a,b)$$

are implied with $\tilde{\xi}$ of order unity, the moving coordinate being defined by

$$X - X_0 = -\tilde{c_1}(T_0 - T)^m + (T_0 - T)^{\tilde{n}}\tilde{\xi}. \qquad (5.9c)$$

Here $\tilde{c_1} \equiv E\hat{L}^3$ is a positive constant, while the index $\tilde{n} > m$, and in addition $3\tilde{q} = \tilde{n} - m + 1$, $3\tilde{r} = \tilde{n} - 2 + 2m$. Substitution into the governing system (4.9), (4.10) shows that the local controlling equations are now

$$\alpha m\tilde{c_1}\tilde{f}^3\tilde{c}' = \tilde{c}, \quad \alpha\tilde{c}' = -m\tilde{c_1}\tilde{f}', \qquad (5.10a,b)$$

so that from (5.10b) $\tilde{c} = \tilde{\lambda}(\tilde{c_2} - \tilde{f})$ for some constant $\tilde{c_2}$ of integration, with $\tilde{\lambda} \equiv m\tilde{c_1}/\alpha$, and (5.10$a$) then yields a nonlinear ordinary differential equation for $\tilde{f}(\tilde{\xi})$. The latter produces the implicit equation

$$\frac{1}{\alpha^2\tilde{\lambda}} \quad \frac{\mathrm{d}\tilde{\xi}}{\mathrm{d}\tilde{f}} = \frac{\tilde{f}^3}{\tilde{f} - \tilde{c_2}} \qquad (5.11)$$

for $\tilde{\xi}(\tilde{f})$ and hence the expression

$$\frac{(\tilde{\xi} - \tilde{\xi}_0)}{\alpha^2\tilde{\lambda}} = \tilde{c_2}^3 \ln|\tilde{g}| + 3\tilde{c_2}^2\tilde{g} + \tfrac{3}{2}\tilde{c_2}\tilde{g}^2 + \tfrac{1}{3}\tilde{g}^3, \qquad (5.12a)$$

$$\tilde{g} \equiv \tilde{f} - \tilde{c_2}, \qquad (5.12b)$$

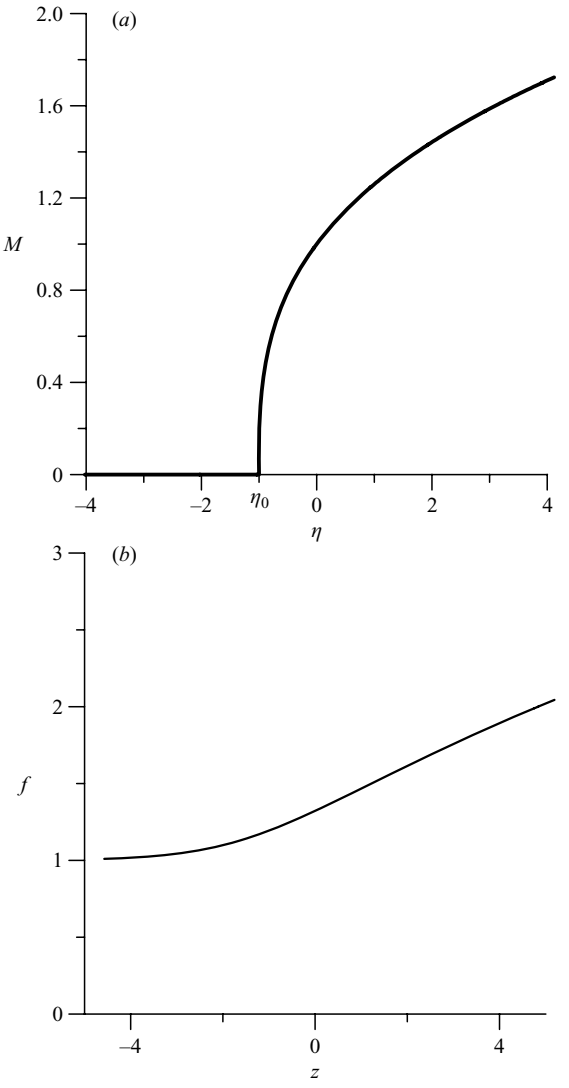

FIGURE 4. Concerning § 5: (*a*) the local touchdown solution for M versus η; (*b*) the behaviour near $\eta = \eta_0$. Here $f \equiv \tilde{f}/\tilde{c_2}$ and $Z \equiv (\tilde{\xi} - \tilde{\xi_0})/(\alpha^2\tilde{\lambda}\tilde{c_2}^3) - \ln \tilde{c_2}$.

from which the acceptable single-valued function $\tilde{f}(\tilde{\xi})$ can be deduced: see figure 4. The smoothing-zone solution (5.12*a*, *b*) matches with (5.8*a*) as $\xi \to \infty$, since (5.12*a*) gives $\tilde{f} \sim (3\tilde{\xi}/\alpha^2\tilde{\lambda})^{1/3}$ and since the factors present in (5.1), (5.3) come into play with (5.8*a*). The smoothing-zone solution also matches as required with (5.8*b*) as $\xi \to -\infty$, in the sense that $\tilde{f}$ then tends to the positive constant value $\tilde{c_2}$ from above, leaving $F \ll (T_0 - T)^{1/3}$ for $\eta < \eta_0$, and simultaneously $\tilde{c}$ becomes exponentially small, leaving $|c| \ll (T_0 - T)^{\theta}$ for $\eta < \eta_0$. The result

$$\min(F) \sim \tilde{c_2}(T_0 - T)^{\tilde{q}}, \tag{5.13}$$

in particular, is the inferred minimum value of the interface shape function F as touchdown approaches.

The solution for M and $\tilde{f}$ in figure 4 essentially gives the local gap shape F in scaled form, in view of (5.1), (5.3), while the local pressure gradient $\partial P/\partial X$ follows as being proportional to N/M^3. (To be precise, we have $\partial P/\partial X = q = c/F^3 = (T_0 - T)^{\tilde{\kappa}} D/f^3 = (T_0 - T)^{\tilde{\kappa}} |D(0)| \alpha\theta N/m^3$, where the power $\tilde{\kappa} = m - 5/3$, from the working in § 4.2 and from (5.1), (5.3).) The left-hand touchdown is similar to the right-hand one and is its mirror image. The same M–N system can be obtained from analysis of (2.5), (2.6), it is important to note, but with an arbitrary constant of integration present. The fact that the latter constant is zero shows that the symmetry plane has a global influence on the local touchdown properties.

To conclude, then, the main findings are that a touchdown occurs at a finite time T_0 and that the power m involved is $m = 1$. Associated comparisons, physical interpretation and applications are to be discussed in the next section.

6. Further comments

6.1. *Comparisons and physical interpretation*

The dynamics of the air–water interaction and consequent approach to touchdown are encapsulated in the equations, analysis and computations of the previous three sections, which are to be compared below. The main points we would draw out immediately in a physical discussion of the dynamics are the following.

First, the balance inherent in the ratio of typical lengths a^*/L^* (where a^*, L^* represent the local and global length scales in turn) and the ratio ρ_2^*/ρ_1^* (for water density ρ_1^* and air density ρ_2^*), both being small of respective orders h, $h^3 Re_1$, is physically important because the disparity in those length scales and densities each affect the dominant dynamics at the same order. The ratio of viscosities μ_2^*/μ_1^* likewise influences the dynamics at that order, in contrast with surface tension effects which are negligible here (although of importance in many other situations). These disparities give rise to the full nonlinear interaction between the quasi-inviscid water layer motion and the quasi-lubricating air layer motion (§ 3), over the range of Reynolds numbers Re_1 of current interest. Second, the lubricant–air layer displays the classical role in the centre of the interaction at the symmetry line (§ 4) where gap closure is prevented, but on either side of that the two-fluid interaction forces the water to continue descending. This process is reinforced in a non-classical manner, as described at the beginning of § 5, and leads to touchdown within a finite scaled time. Third, the part played by the flexibility of the water layer at the interface as described at the end of § 3, i.e. full nonlinear interaction, should be highlighted, as it is the root cause of the touchdown.

Comparisons between the time-marched numerical results of § 3 and the analytical findings of § 4, and § 5 indicate that there is a close measure of qualitative agreement at least. Concerning the symmetry station first, the decrease with scaled time of the scaled air gap thickness F there in the computations is eventually slow compared with that at other stations, and this is a feature which is exactly in keeping with the change in sign of the gap curvature described in § 4. The descent in the symmetry station thickness is indeed virtually halted near the end of the computations, with F then being just below 2.5: that value ties in reasonably with the analytical prediction (4.6), which gives the terminal result as $\sqrt{6}$. Second, as far as touchdown is concerned we see that, no matter whether the left-hand or the right-hand touchdown is being considered, viewed locally, the side of the F graph on which the minimum of F occurs is all 'lower' than the other side throughout the time-marching computational

solutions. Such a relationship agrees with the analytical results in § 5; in fact the whole shape of the curve in figure 4 for M or f, which is proportional to F, is qualitatively the same as in the time-marched computations, while the sensitive growth in the scaled pressure near touchdown is as § 5 implies, all of which are further encouraging features. Again, the value of the power m in the local theory is suggested as unity by comparison with the non-local properties. So, in particular, the scaled pressure behaves (to within an additive constant) as the displaced scaled time $T_0 - T$ to the power $2m-5/3$, which is a comparatively small positive power implying comparatively slow growth in the local pressure gradient as touchdown is approached, in line with the computations shown in figure 2(d). This leaves us then with the results

$$F \sim \{(X - X_0) - c\,(T - T_0)\}^{1/3}, \quad P \sim \text{constant} + O\,\{(X - X_0) - c\,(T - T_0)\}^{1/3} \quad (6.1)$$

for the local shape and pressure responses on one side near touchdown at the time $T = T_0$ and location $X = X_0$, with the constant c acting as an effective approach speed at touchdown; the other side near touchdown has F being much smaller, as in (5.12). The minimum gap width as touchdown is approached is predicted by (5.13), where $\widetilde{q} = (\tilde{n} - m + 1)/3$ and $\tilde{n} > m$. For m of unity and (say) $\tilde{n} = 3$, this gives a minimum gap width tending to zero linearly with the scaled time T as the touchdown time T_0 is approached, a prediction which is consistent, or at least not inconsistent, with the results in figure 2(b, d) for the time-marched computations. The reason for considering (5.13) as a minimum, near the scaled touchdown station $X = X_0$, is that as an asymptote holding for large negative values of the scaled local coordinate it matches with the exact solution $F = \widetilde{c_2}(X_0 - X)^{\tilde{q}}/\widetilde{c_1}^{\tilde{q}}$ in the bulk of the motion as $X - X_0$ becomes 0(1) and negative ($\widetilde{c_1}, \widetilde{c_2}$ are constants), or more widely with the simple exact solution $F = F_0(X), c = 0$ of (4.9), (4.10), where $F_0(X)$ is any arbitrary function of the scaled coordinate X.

The computations and the analyses seem to fit together then. We should remark here immediately that the § 4 analysis continues holding true for all scaled time T in principle, whereas § 5, like the computations, has touchdown occurring within a finite scaled time. The global influence on that touchdown is also interesting and perhaps somewhat surprising, with the flow behaviour at the symmetry station, in particular, having an explicit influence on the behaviour at the remote touchdown stations, as explained in detail in § 4. Travelling wave solutions of the controlling equations in § 2 or the equivalent ones in § 4 can also be derived, but these are considered as less significant in the light of the implied touchdowns. Taken altogether, air trapping between the two touchdown locations seems to be confirmed and, moreover, subsequent touchdowns would tend to lead to further pockets of air being formed, quite possibly of a similar extent along the surface.

Surface tension has a well-known influence, as described by Purvis & Smith (2004*b*), among others, in the present situation of large Weber numbers, where it provokes significant distortion of the interface when large curvatures develop, as they do at touchdown. This influence is one among several new physical factors that come into play locally then. In further terms of physical insight we should add that there is no novelty in identifying air trapping itself, which is a quite frequently observed occurrence, but there is novelty, we believe, in identifying the current air–water interaction as one mechanism for air trapping on a relatively small scale as a very common recurrence (due to two-pronged touchdown). Moreover, in the more realistic three-dimensional but axisymmetric counterpart of the present scenario, the touchdown features of § 5 still apply in full, simply because the touchdown is so

localized away from the symmetry line (or axis) that it yields quasi-two-dimensional physical dynamics there. Thus the applications are widespread in principle.

6.2. *Applications*

Various applications involving impacts provide the background motivations for the study, as mentioned in some detail in the Introduction, and the controlling system that emerges additionally models elastic-wall effects on a thin fluid layer. It should be stressed, however, that the double-fluid squeeze process and the accompanying pressure-shape interaction law inherent in the current work do not cover directly the application to droplet impact on water, which is the relatively deep-water setting, because another pressure-shape interaction then dominates and the present thin-coat effect is absent. Nevertheless, the present thin-coat law does in some sense replicate the deep-water law addressed in Smith *et al.* (2003), or rather mimics its behavioural influence, similar to the aerodynamic- and internal-flow mimicry in interacting boundary layers. The touchdown form in § 5 is quite similar in detail to that in the above paper, for instance. The replication here adds weight to the finding of touchdown in that paper.

Concerning the bouncing phenomena and interactions observed by Protiere *et al.* (2006) (see also Pan and Law 2007), it would be interesting to explore whether or not the theory of the current paper could perhaps apply to the above phenomena, given that the dynamics of the thin film of air squeezed between the drop and the liquid bath underneath are shown in Couder *et al.* (2005a,b) to play a key part. Protiere *et al.* also present an averaged simple theoretical approach which reproduces many of the observed phenomena, and so our aim would partly be to complement their approach as well as to add to the understanding of the fascinating phenomena involved. We also draw the reader's attention to the rather secondary pressure peak in figure 2(*d*), which appears to be similar to the spike in elastohydrodynamic lubrication problems as described by Afandizadeh Zargari *et al.* (2007), for example.

Sport-related applications are of particular interest. In approximate terms, a football of diameter 300 mm, say, might approach the ground with speed 12 m s^{-1}, yielding a water-based global Reynolds number Re_1 of around 2 million. This value is well below the critical value of 10 million and so indicates application of the present subcritical theory. A representative value for the parameter h is then 0.01, in line with the assumptions of the theory, and that points to air–pockets of length 3 mm being formed on the football during its impact with the ground in the presence of water layers of depth less than 3 mm. A tennis ball is smaller in diameter by a factor of about 4 and its speeds might be greater by a factor of 3; therefore Re_1 is comparatively little different from the estimate above, and on that basis the present theory again applies. Representative air pocket lengths in this case are predicted as about 1 mm. Next, for a golf ball the diameter reduction is perhaps by a factor 10 relative to the football, whereas the speed increase gives a factor of around 5. Hence again the Re_1 estimate is altered relatively little (the range involved is even more subcritical), and in principle the present treatment still holds, yielding air pocket lengths now of about 0.3 mm. These sports applications can be contrasted with that of the approach of an ice particle to an aircraft wing, where the typical diameter might be 0.5 mm and speed 100–400 m/sec^{-1}. There the water-based global Reynolds number is considerably smaller than above, the subcritical theory is indicated as being yet more relevant, and representative air pocket lengths of 5 microns are indicated.

Another matter of some concern is the relation of the current findings for the subcritical range to the properties in the unsteady interactive boundary layer regime

(Smith 1988) which applies in the critical Reynolds number range, although that critical value of $(\rho_1^{*2}\nu_2^*)/(\rho_2^{*2}\nu_1^*)$ is high compared with the Reynolds numbers of industrial interest. The crossover to an inviscid–inviscid interaction follows at still higher Reynolds numbers, but then the interaction turns out to be very unstable. Another different aspect concerns new physics, including the new physics that must enter the reckoning on smaller time and length scales closer to touchdown, where, in addition to the points made by Smith *et al.* (2003), the non-thinness of the interactive flow in the latter work may re-enter play. In the present setting, if the typical water coat is even shallower than those examined here then viscous effects could be amplified. Improved application and further interest would suggest considering substantial obliqueness effects (previous works demonstrate that obliqueness must be very substantial if a spatially symmetric interactive setting of the present type is to be altered), as well as gravity, surface tension, density effects and three-dimensionality, as in the Appendix, while the industrial context of an incident ice lump mentioned in the Introduction points to roughness playing a significant role.

Thanks are due from A.S.E. and F.T.S. to Roger Gent and colleagues at QinetiQ for their interest and support. A.A.K. is grateful to the Russian Fund of Basic Research (grant 07-08-00145) for support. Further thanks are also due to EPSRC for financial support of A.A.K. through a Visiting Fellowship at UCL, and of A.S.E. through a postdoctoral grant. Very helpful comments from the editor and referees are gratefully acknowledged.

Appendix. Three-dimensional, compressible, viscous and other effects

There are many physical factors which may be involved in air–water interaction apart from the major ones encapsulated in (2.5), (2.6), and so this Appendix examines in some detail such factors for the current scenarios and applications to check that they are indeed secondary effects as assumed. The appendix describes the three-dimensional setting first, followed in turn by the behaviour at times significantly prior to impact, the behaviour and air–water interaction on the verge of impact, numerical estimates of the parameters involved, the dominant physical effects that emerge, the relevant boundary conditions and reduced governing equations, and final checks and comments.

A.1. *The three-dimensional setting*

For a rigid elliptic paraboloid approaching a horizontal plane covered with a thin liquid layer, the body surface in dimensional form is described by

$$y^* = \frac{x^{*2}}{2R_x^*} + \frac{z^{*2}}{2R_z^*} - V^* t^* \quad (t^* < 0), \tag{A1}$$

where $R_x^* \leqslant R_z^*$, and (to repeat) an asterisk denotes a dimensional quantity. This body shape is three-dimensional and typical. The surface of the moving body can also be covered with water, although we restrict ourselves here to a dry rigid body approaching a wet horizontal plane. The free surface of the liquid layer is initially flat, $y^* = 0$, and its bottom is in the plane $y^* = -H_b^*$, say. For numerical estimates as in the main text we consider a layer of water on the flat plane and air above the water, with R_x^*, H_b^* and V^* being the main parameters and the ratio $\epsilon = \rho_a^*/\rho_\ell^*$ being a small parameter, about 0.001 for the air–water system. The subscripts ℓ, a are equivalent, respectively, to 1, 2 (liquid, air) as used earlier. In the following we assume that

the body velocity is relatively high, so that the Reynolds numbers $Re_a = V^* R_x^*/\nu_a^*$ of the air flow and $Re_\ell = V^* R_x^*/\nu_\ell^*$ of the liquid flow are both large, where the representative length scale L^* is R_x^* effectively. For the air–water system we have $\nu_a^* = 1.32 \times 10^{-5}$ m^2 s^{-1}, $\nu_\ell^* = 0.18 \times 10^{-5}$ m^2 s^{-1}, $\rho_a^* = 1.29$ kg m^{-3}, $\rho_\ell^* = 1000$ kg m^{-3} at temperature 0°C. The ratio $æ \equiv \nu_a^* \rho_a^*/(\nu_\ell^* \rho_\ell^*)$ is 0.00946 for that system.

During the time stage of possible touchdown, the deflection of the air–water surface is comparable with the thickness of the air gap and the water surface may almost touch the surface of the body eventually, trapping an air pocket. The water surface deflection is caused by the air flow in the gap and the aerodynamic pressure, which tends to increase with decreasing air gap.

A.2. *Significantly before impact*

When the body is relatively far from the water surface, the aerodynamic pressure over the water surface is of the order of $\rho_a^* V^{*2}$, which is the pressure scale for the body motion in unbounded fluid, the air flow being three-dimensional with velocity of the order of the body velocity V^*. The air gap during this non-interactive stage has length of the order of R_x^*, and the time scale T^* can then be estimated with the help of (A1) as R_x^*/V^*. The spatial variables x^*, y^* and z^* are all of order R_x^*. The pressure gradient on the water surface is thus of order $\rho_a^* V^{*2}/R_x^*$ and initiates horizontal flow in the liquid layer with acceleration $\rho_\ell^{*-1} \rho_a^* V^{*2}/R_x^*$. The corresponding horizontal velocity scale, obtained as the product of the liquid acceleration and the time scale T^*, is therefore $T^* \rho_\ell^{*-1} \rho_a^* V^{*2}/R_x^* = \epsilon V^*$. The continuity equation, where the horizontal scale is R_x^* but the vertical scale is H_b^*, provides the order of the liquid vertical velocity as $\epsilon V^* H_b^*/R_x^*$, if $H_b^* \ll R_x^*$, or ϵV^*, if H_b^* is $O(R_x^*)$.

The water surface deflection can now be estimated as the product of the liquid vertical velocity by the time scale, giving $T^* \epsilon V^* = \epsilon R_x^*$ for deep water and $T^* \epsilon V^* H_b^*/R_x^* = \epsilon H_b^*$ for a shallow liquid layer. It is seen that in both cases the water surface deflections for this stage are very small and can be neglected in considering the body motion in air, when the distance between the body surface and the liquid layer is comparable with the characteristic linear dimension of the body. (Therefore, in the case of the air–water system the deflection of the liquid surface can be neglected with a relative accuracy of $O(\epsilon)$ for deep liquid, when the body is not close to the liquid. In the case of a shallow liquid layer the liquid surface deflections are even less than those for deep water). The viscous effects (see also Smith *et al.* 2003) can be neglected in both the air and the liquid once the Reynolds numbers Re_a and Re_ℓ are large, which is a main assumption of the present appendix. Viscous effects can be estimated with the help of boundary layer theory. The compressibility of the air can be neglected if the body velocity is much smaller than the sound speed c_a^* in the air at rest. For air, $c_a^* = 330$ m s^{-1}. It is assumed that the body is moving smoothly, so that weak shock waves are not generated by its motion. If the body velocity is significantly smaller than the sound speed c_a^* in the air, the liquid can also be treated as incompressible. It is important to notice that the nonlinear terms in the equations of the liquid motion (but not in the equations of the air flow) can be neglected with the relative accuracy $O(\epsilon)$. We conclude that during the stage under consideration both the air and the liquid can be treated as incompressible ideal fluids, the air flow can be obtained to leading order as $\epsilon \ll 1$ without accounting for deflection of the liquid surface. The liquid surface can be approximately replaced with a rigid flat plane. After the aerodynamic pressure over this plane has been computed, one can calculate the liquid motion and find the liquid surface deflection in the leading order

by solving the linear problem of liquid layer motion due to given external pressure distribution. This asymptotic analysis is valid not only for elliptic paraboloid (A1) but for any body shape. It is seen that during the non-interactive stage the air flow and the liquid flow are decoupled and can be computed one after another.

A.3. *On the verge of impact*

The flow patterns change when the body is in close proximity to the liquid surface. With the small non-dimensional parameter δ_a characterizing the distance of the body from the initially undisturbed liquid surface, so that $\delta_a \sim h$ in the main text, we use coordinates, velocity components and pressure,

$$y^* = R_x^* \delta_a^2 y_2, \quad x^* = R_x^* \delta_a X, \quad z^* = R_x^* \delta_a Z, \quad t^* = (R_x^*/V^*)\delta_a^2 T, \tag{A2}$$

$$u_x^{*(a)} = V^* \delta_a^{-1} \tilde{u}_x^{(a)}, \quad u_z^{*(a)} = V^* \delta_a^{-1} \tilde{u}_z^{(a)}, \quad u_y^{*(a)} = V^* \tilde{u}_y^{(a)}, \tag{A3}$$

$$p^{*(a)} = \rho_a^* V^{*2} Q \tilde{p}^{(a)}, \tag{A4}$$

respectively, similar to § 2. Equations (A2) follow from (A1), which should be non-trivial in non-dimensional variables. Correspondingly, the scalings (A3) come from the continuity equation in the air flow and the constraint that this equation written in non-dimensional variables must be non-trivial as $\delta_a \to 0$. In (A4) the factor Q will be obtained as a part of the asymptotic analysis. In non-dimensional variables (A1) takes the form

$$y_2 = \tfrac{1}{2}[X^2 + \mu^2 Z^2] - T, \tag{A5}$$

where $\mu^2 = R_x^*/R_z^*$, $0 \leqslant \mu \leqslant 1$. The Navier–Stokes equations for the air flow between the liquid surface and body surface (A5) have the forms (with $\tilde{x}$, $\tilde{y}$, $\tilde{z}$, $\tilde{t}$ written for X, y_2, Z, T)

$$\delta_a^{-2} \frac{\partial \tilde{u}_x^{(a)}}{\partial \tilde{t}} = -Q \frac{\partial \tilde{p}^{(a)}}{\partial \tilde{x}} + \frac{1}{Re_a \delta_a^4} \left[\frac{\partial^2 \tilde{u}_x^{(a)}}{\partial \tilde{y}^2} + \delta_a^2 \Delta_2 \tilde{u}_x^{(a)} \right], \tag{A6}$$

$$\delta_a^{-2} \frac{\partial \tilde{u}_z^{(a)}}{\partial \tilde{t}} = -Q \frac{\partial \tilde{p}^{(a)}}{\partial \tilde{z}} + \frac{1}{Re_a \delta_a^4} \left[\frac{\partial^2 \tilde{u}_z^{(a)}}{\partial \tilde{y}^2} + \delta_a^2 \Delta_2 \tilde{u}_z^{(a)} \right], \tag{A7}$$

$$\frac{\partial \tilde{u}_y^{(a)}}{\partial \tilde{t}} = -Q \frac{\partial \tilde{p}^{(a)}}{\partial \tilde{y}} + \frac{1}{Re_a \delta_a^2} \left[\frac{\partial^2 \tilde{u}_y^{(a)}}{\partial \tilde{y}^2} + \delta_a^2 \Delta_2 \tilde{u}_y^{(a)} \right], \tag{A8}$$

$$\frac{\partial \tilde{u}_x^{(a)}}{\partial \tilde{x}} + \frac{\partial \tilde{u}_y^{(a)}}{\partial \tilde{y}} + \frac{\partial \tilde{u}_z^{(a)}}{\partial \tilde{z}} = 0. \tag{A9}$$

In (A6)–(A9) we do not account for the gravity force or for air compressibility: see later, where we derive the conditions of the motion under which the air can be treated as an incompressible fluid. Here $\Delta_2 = \partial^2/\partial \tilde{x}^2 + \partial^2/\partial \tilde{y}^2$. The terms with Δ_2 in (A6)–(A8) can be neglected at leading order with a relative accuracy $O(\delta_a^2)$ as $\delta_a \to 0$.

The air flow equations (A6)–(A9) are of the most non-trivial forms as $\delta_a \to 0$ when $Re_a \delta_a^2 = O(1)$. In this case, $Q = \delta_a^{-2}$ and (A6)–(A9) take to leading order the forms

$$\frac{\partial \tilde{u}_x^{(a)}}{\partial \tilde{t}} = -\frac{\partial \tilde{p}^{(a)}}{\partial \tilde{x}} + \frac{\partial^2 \tilde{u}_x^{(a)}}{\partial \tilde{y}^2}, \quad \frac{\partial \tilde{u}_z^{(a)}}{\partial \tilde{t}} = -\frac{\partial \tilde{p}^{(a)}}{\partial \tilde{z}} + \frac{\partial^2 \tilde{u}_z^{(a)}}{\partial \tilde{y}^2}, \tag{A10}$$

$$\frac{\partial \tilde{p}^{(a)}}{\partial \tilde{y}} = 0, \quad \frac{\partial \tilde{u}_x^{(a)}}{\partial \tilde{x}} + \frac{\partial \tilde{u}_y^{(a)}}{\partial \tilde{y}} + \frac{\partial \tilde{u}_z^{(a)}}{\partial \tilde{z}} = 0. \tag{A11}$$

Let us now check the conditions under which a stage of strong interaction between the air flow and the liquid motion corresponds to an air gap thickness with $Re_a\delta_a^2 = O(1)$. In order to perform such an analysis we repeat our reasoning for the early stage with $\delta_a = O(1)$. The liquid flow is initiated by the aerodynamic pressure gradient, which is of the order of $\rho_a^* V^{*2}\delta_a^{-2}/(R_x^*\delta_a)$. The acceleration of the horizontal flow in the liquid layer is of the order of $\rho_\ell^{*-1}\rho_a^* V^{*2}\delta_a^{-3}/R_x^*$. The corresponding horizontal velocity scale is obtained as the product of the liquid acceleration by the time scale $T^* = (R_x^*/V^*)\delta_a^2$, which is $T^*\epsilon V^{*2}\delta_a^{-3}/R_x^* = \epsilon\delta_a^{-1}V^*$. The continuity equation, where the horizontal scale is $R_x^*\delta_a$ and the vertical scale is H_b^*, provides the order of the vertical liquid velocity as $\epsilon\delta_a^{-2}V^*H_b^*/R_x^*$, if $H_b^* \ll R_x^*\delta_a$, and $\epsilon\delta_a^{-1}V^*$ for deep water where $H_b^* = O(R_x^*\delta_a)$ or greater. The water surface deflection can be estimated as the product of the liquid vertical velocity by the time scale, which is $T^*\epsilon\delta_a^{-1}V^* = \epsilon\delta_a R_x^*$ for deep water and ϵH_b^* for a shallow liquid layer. Note that the liquid layer can be treated as shallow if $H_b^* \ll R_x^*\delta_a$. The deflection of the liquid surface is of the order of the air gap thickness $V^*T^* = R_x^*\delta_a^2$ when $\epsilon\delta_a R_x^* = R_x^*\delta_a^2$ for deep water, which gives $\delta_a = \epsilon$, and when $\epsilon H_b^* = R_x^*\delta_a^2$ for shallow water, which gives $\delta_a = \sqrt{\epsilon H_b^*/R_x^*}$. The inequality $H_b^* \ll R_x^*\delta_a$ implies that strong interaction between the air flow and the liquid layer occurs at a smaller air gap thickness for a shallow liquid layer than for a deep layer.

A.4. *Numerical estimates*

In this general case the asymptotic equation $Re_a\delta_a^2 = O(1)$ is satisfied when $V^*R_x^* \sim \nu_a^*\epsilon^{-2}$ for a deep layer, $\epsilon R_x^*/H_b^* = O(1)$, and when $V^*H_b^* \sim \nu_a/\epsilon$ for a shallow layer, $H_b^* \ll \epsilon R_x^*$. For the air–water system we find $V^*R_x^* \sim 13.2$ m^2 s^{-1} for a deep layer and $V^*H_b^* \sim 0.00132$ m^2 s^{-1} for a shallow layer, where $H_b^* \ll R_x^*/1000$. For example, for $R_x^* = 1$ m the body velocity should be of the order of 10 m s^{-1} and the liquid layer can be treated as deep once H_b^* is greater than 1 mm.

The asymptotic analysis presented is still valid if $Re_a\delta_a^2 \gg 1$, but now the air can be treated as an ideal fluid, i.e. the second-order derivatives in (A10) can be neglected at leading order. Other scales remain unchanged. In this case we have $V^*R_x^* \gg 13.2$ m^2 s^{-1} for a deep layer, which implies that this case corresponds to large bodies and high speeds of their motion.

For small bodies the stage of strong interaction starts for a very small air gap thickness and its duration is very small. This corresponds to the inequality $Re_a\delta_a^2 \ll 1$. Equations (A6) and (A7) show that $Q = 1/Re_a\delta_a^4$ and the inertia terms can be neglected, so that we arrive at the equations of quasi-stationary lubrication theory. The asymptotic analysis of the liquid surface deflection, which is similar to that demonstrated above, shows that the liquid surface deflection is of the order of the air gap thickness when $\delta_a^3 = \epsilon/Re_a$ for a deep liquid layer and $\delta_a^4 = \epsilon H_b^*/(R_x^*Re_a)$ for a shallow liquid layer. The liquid layer can be treated as shallow when $(H_b^*/R_x^*)^3 \ll \epsilon/Re_a$. The inequality $Re_a\delta_a^2 \ll 1$ gives $Re_a\epsilon^2 \ll 1$ for a deep layer and $Re_a\epsilon H_b^*/R_x^* \ll 1$ for a shallow liquid layer. These inequalities correspond to the restrictions $V^*R_x^* \ll \nu_a^*\epsilon^{-2}$ for a deep layer and $V^*H_b^* \ll \nu_a^*/\epsilon$ for a shallow layer, $(H_b^*/R_x^*)^3 \ll \epsilon/Re_a$. It is seen that this case corresponds to bodies of small dimension such as water drops.

A.5. *The dominant effects*

In this paper we restrict ourselves to the last case mentioned, where the viscous effects are of major importance and inertia terms do not matter. In this case (A10) and (A11) are approximated as

$$\frac{\partial\tilde{p}^{(a)}}{\partial\tilde{x}} = \frac{\partial^2\tilde{u}_x^{(a)}}{\partial\tilde{y}^2}, \quad \frac{\partial\tilde{p}^{(a)}}{\partial\tilde{z}} = \frac{\partial^2\tilde{u}_z^{(a)}}{\partial\tilde{y}^2}, \quad \frac{\partial\tilde{p}^{(a)}}{\partial\tilde{y}} = 0, \quad \frac{\partial\tilde{u}_x^{(a)}}{\partial\tilde{x}} + \frac{\partial\tilde{u}_y^{(a)}}{\partial\tilde{y}} + \frac{\partial\tilde{u}_z^{(a)}}{\partial\tilde{z}} = 0. \qquad \text{(A12)}$$

The no-slip conditions on the body surface $\tilde{z} = f(\tilde{x}, \tilde{y}) - \tilde{t}$ are

$$\tilde{u}_x^{(a)} = 0, \quad \tilde{u}_z^{(a)} = 0, \quad \tilde{u}_y^{(a)} = -1, \tag{A13}$$

and the kinematic condition on the liquid surface $\tilde{y} = \tilde{\eta}(\tilde{x}, \tilde{z}, \tilde{t})$ has the form

$$\tilde{u}_y^{(a)} = \tilde{u}_x^{(a)} \frac{\partial \tilde{\eta}}{\partial \tilde{x}} + \tilde{u}_z^{(a)} \frac{\partial \tilde{\eta}}{\partial \tilde{z}} + \frac{\partial \tilde{\eta}}{\partial \tilde{t}}. \tag{A14}$$

Now we analyse the liquid motion in the thin layer. Note that the definition of the 'thin layer' should be given. The characteristic horizontal length of the air flow is $R_x^* \delta_a$, which is why we expect that the liquid equations can be considered within the 'thin layer' approximation (or, within the shallow-water approximation, which is the same) if $H_b^* \ll R_x^* \delta_a$. Taking into account that, for a shallow liquid layer $\delta_a^4 = \epsilon H_b^*/(R_x^* Re_a)$, the asymptotic inequality $H_b^* \ll R_x^* \delta_a$ gives $H_b^*/R_x^* \ll [\epsilon/Re_a]^{1/3}$. Moreover, we consider the case where $Re_a \delta_a^2 \ll 1$, which leads to the inequality $H_b^*/R_x^* \ll 1/[\epsilon/Re_a]$. We conclude that the air flow is governed by viscous effects, and the liquid flow is shallow if

$$H_b^*/R_x^* \ll \min\{1/[\epsilon Re_a], [\epsilon/Re_a]^{1/3}\}. \tag{A15}$$

The ratio

$$\frac{[\epsilon/Re_a]^{1/3}}{1/[\epsilon Re_a]} = (Re_a \epsilon^2)^{2/3}$$

is smaller than unity if $V^* R_x^* \ll \nu_a^* \epsilon^{-2}$.

In the dynamic boundary condition on the air–water interface we do not account for surface tension, which is why in the present analysis the dynamic boundary condition implies that the pressure is continuous at the interface. The conditions under which surface tension can be neglected will be obtained at the end of this Appendix.

In the case under consideration we introduce the non-dimensional variables in the equations of the liquid water flow as

$$y^* = H_b^* Y, \quad x^* = R_x^* \delta_a X, \quad z^* = R_x^* \delta_a Z, \quad t^* = (R_x^*/V^*)\delta_a^2 T, \tag{A16}$$

$$u_x^{*(\ell)} = (V^* R_x^* \delta_a / H_b^*) \bar{u}_x^{(\ell)}, \quad u_y^{*(\ell)} = (V^* R_x^* \delta_a / H_b^*) \bar{u}_y^{(\ell)}, \quad u_z^{*(\ell)} = V^* \tilde{u}_z^{(\ell)}, \tag{A17}$$

$$p^{*(\ell)} = P_{sc}^* \tilde{p}^{(\ell)}, \quad P_{sc}^* = \frac{\rho_a^* V^{*2}}{Re_a \delta_a^4}, \tag{A18}$$

for the coordinates, velocity components and pressure in turn. The horizontal coordinates and time are scaled in the same way as for the air flow. Also, the vertical components of the air and liquid velocity are both scaled with the body velocity V^*, in this stage during which the elevation of the free surface is of the order of the air gap thickness $R_x^* \delta_a^2$. The scale of the horizontal components of the liquid velocity comes from the continuity equation and the condition that the horizontal flow of the liquid is driven by the gradient of the induced aerodynamic pressure, which acts over the free surface of the liquid layer.

The Navier–Stokes equations of the liquid flow in non-dimensional variables now have the forms

$$\frac{\partial \bar{u}_x^{(\ell)}}{\partial \tilde{t}} + \mu \left[\bar{u}_x^{(\ell)} \frac{\partial \bar{u}_x^{(\ell)}}{\partial \tilde{x}} + \bar{u}_z^{(\ell)} \frac{\partial \bar{u}_x^{(\ell)}}{\partial \tilde{z}} + \tilde{u}_y^{(\ell)} \frac{\partial \bar{u}_x^{(\ell)}}{\partial \bar{y}} \right] = -\frac{\partial \tilde{p}^{(\ell)}}{\partial \tilde{x}} + \frac{\mu^3}{æ} \left[\frac{\partial^2 \bar{u}_x^{(\ell)}}{\partial \bar{y}^2} + \lambda^2 \Delta_2 \bar{u}_x^{(\ell)} \right], \tag{A19}$$

$$\frac{\partial \bar{u}_z^{(\ell)}}{\partial \tilde{t}} + \mu \left[\bar{u}_x^{(\ell)} \frac{\partial \bar{u}_z^{(\ell)}}{\partial \tilde{x}} + \bar{u}_z^{(\ell)} \frac{\partial \bar{u}_z^{(\ell)}}{\partial \tilde{z}} + \tilde{u}_y^{(\ell)} \frac{\partial \bar{u}_z^{(\ell)}}{\partial \bar{y}} \right] = -\frac{\partial \tilde{p}^{(\ell)}}{\partial \tilde{z}} + \frac{\mu^3}{æ} \left[\frac{\partial^2 \bar{u}_z^{(\ell)}}{\partial \bar{y}^2} + \lambda^2 \Delta_2 \bar{u}_z^{(\ell)} \right], \tag{A20}$$

$$\frac{\partial \tilde{u}_y^{(\ell)}}{\partial \tilde{t}} + \mu\left[\bar{u}_x^{(\ell)}\frac{\partial \tilde{u}_y^{(\ell)}}{\partial \tilde{x}} + \bar{u}_z^{(\ell)}\frac{\partial \tilde{u}_y^{(\ell)}}{\partial \tilde{z}} + \tilde{u}_y^{(\ell)}\frac{\partial \tilde{u}_y^{(\ell)}}{\partial \bar{y}}\right] = -\frac{1}{\lambda^2}\frac{\partial \tilde{p}^{(\ell)}}{\partial \bar{y}} + \frac{\mu^3}{æ}\left[\frac{\partial^2 \tilde{u}_y^{(\ell)}}{\partial \bar{y}^2} + \lambda^2 \Delta_2 \tilde{u}_y^{(\ell)}\right], \tag{A21}$$

$$\frac{\partial \bar{u}_x^{(\ell)}}{\partial \tilde{x}} + \frac{\partial \bar{u}_y^{(\ell)}}{\partial \tilde{y}} + \frac{\partial \tilde{u}_z^{(\ell)}}{\partial \bar{z}} = 0, \tag{A22}$$

where (X, Y, Z, T) are written $(\tilde{x}, \bar{y}, \tilde{z}, \tilde{t})$ and

$$\mu = \left(\frac{\epsilon R_x^*}{Re_a H_b^*}\right)^{1/2}, \quad \lambda = \frac{H_b^*}{R_x^* \delta_a}, \quad æ = \frac{\nu_a^* \rho_a^*}{\nu_\ell^* \rho_\ell^*}. \tag{A23}$$

Here $\lambda \ll 1$ and μ is the ratio between the thickness of the air gap $R_y^* \delta_a^2$ and the liquid layer depth H_b^*. We consider the case where $\mu \ll 1$ and $\mu^3/æ \ll 1$. In this case both the viscous terms and nonlinear terms in (A19)–(A22) can be neglected at leading order. Taking into account that $æ \ll 1$, we conclude that these inequalities are satisfied if $\mu \ll æ^{1/3}$, which gives

$$\frac{H_b^*}{R_x^*} \gg \frac{\epsilon}{Re_a} æ^{-2/3}. \tag{A24}$$

Combining (A15) and (A24), we find that the liquid flow can be treated within the shallow-water approximations as ideal and linear if

$$\frac{\epsilon}{Re_a æ^{\frac{2}{3}}} \ll \frac{H_b^*}{R_x^*} \ll \left(\frac{\epsilon}{Re_a}\right)^{1/3}. \tag{A25}$$

Such a range of ratios H_b^*/R_x^* exists if and only if $\epsilon Re_a^{-1} æ^{-2/3} \ll \epsilon^{1/3} Re_a^{-1/3}$. By using the definitions of ϵ, Re_a and æ, this inequality can be presented in an equivalent form as $Re_\ell \gg 1$, which gives $V^* R_x^* \gg \nu_l^*$. The latter inequality is satisfied in many practical problems.

Letting μ and λ in (A19)–(A22) tend to zero, we arrive at the linear shallow-water equations of the liquid flow,

$$\frac{\partial \bar{u}_x^{(\ell)}}{\partial \tilde{t}} = -\frac{\partial \tilde{p}^{(\ell)}}{\partial \tilde{x}}, \quad \frac{\partial \bar{u}_z^{(\ell)}}{\partial \tilde{t}} = -\frac{\partial \tilde{p}^{(\ell)}}{\partial \tilde{z}}, \quad \frac{\partial \tilde{p}^{(\ell)}}{\partial \bar{y}} = 0, \tag{A26}$$

$$\frac{\partial \bar{u}_x^{(\ell)}}{\partial \tilde{x}} + \frac{\partial \bar{u}_y^{(\ell)}}{\partial \tilde{y}} + \frac{\partial \tilde{u}_z^{(\ell)}}{\partial \bar{z}} = 0. \tag{A27}$$

The air–water interface in the non-dimensional variables (A16) is described by the equation

$$\bar{y} = \mu \tilde{\eta}(\tilde{x}, \tilde{z}, \tilde{t}),$$

and the kinematic condition on the interface has the form

$$\tilde{u}_y^{(\ell)} = \mu\left(\bar{u}_x^{(\ell)}\frac{\partial \tilde{\eta}}{\partial \tilde{x}} + \bar{u}_z^{(\ell)}\frac{\partial \tilde{\eta}}{\partial \tilde{z}}\right) + \frac{\partial \tilde{\eta}}{\partial \tilde{t}}. \tag{A28}$$

We integrate equation (A27) with respect to $\bar{y}$ from -1 to $\mu\tilde{\eta}(\tilde{x}, \tilde{z}, \tilde{t})$ accounting for the kinematic condition (A28) and the bottom condition $\tilde{u}_z^{(\ell)}(\tilde{x}, -1, \tilde{z}, \tilde{t}) = 0$, and let $\mu \to 0$, which gives

$$\frac{\partial \bar{u}_x^{(\ell)}}{\partial \tilde{x}} + \frac{\partial \bar{u}_z^{(\ell)}}{\partial \tilde{z}} + \frac{\partial \tilde{\eta}}{\partial \tilde{t}} = 0. \tag{A29}$$

Differentiating (A29) in time and using (A26), we obtain

$$\frac{\partial^2 \tilde{p}^{(\ell)}}{\partial \tilde{x}^2} + \frac{\partial^2 \tilde{p}^{(\ell)}}{\partial \tilde{z}^2} = \frac{\partial^2 \tilde{\eta}}{\partial \tilde{t}^2}. \tag{A30}$$

A.6. *Boundary conditions and main equations*

In order to integrate equations (A12), we need the dynamic conditions on the liquid boundary $\bar{y} = \eta(\tilde{x}, \tilde{z}, \tilde{t})$:

$$\boldsymbol{\Pi}^{*(a)}\langle \boldsymbol{n} \rangle = \boldsymbol{\Pi}^{*(\ell)}\langle \boldsymbol{n} \rangle, \tag{A31}$$

where $\boldsymbol{\Pi}^{*(a)}$ and $\boldsymbol{\Pi}^{*(\ell)}$ are stress tensors for the air flow and the liquid flow, respectively, and $\langle \boldsymbol{n} \rangle$ is the unit normal. Here

$$\boldsymbol{n}(\tilde{x}, \tilde{z}, \tilde{t}) = \frac{(-\delta_a \partial\tilde{\eta}/\partial\tilde{x}, -\delta_a \partial\tilde{\eta}/\partial\tilde{z}, 1)}{\sqrt{1 + \delta_a^2 |\nabla\tilde{\eta}|^2}}, \tag{A32}$$

$$\boldsymbol{\Pi}^{*(a)}\langle \boldsymbol{n} \rangle = P_{sc}^* \big[-\tilde{p}^{(a)}\mathbf{n} + \delta_a \mathscr{A}_1\langle \mathbf{n} \rangle + \delta_a^2 \mathscr{A}_2\langle \mathbf{n} \rangle + \delta_a^3 \mathscr{A}_3\langle \mathbf{n} \rangle \big], \tag{A33}$$

P_{sc}^* is given by equation (A18), and

$$\mathscr{A}_1 = \begin{pmatrix} 0 & 0 & \partial\tilde{u}_x^{(a)}/\partial\tilde{y} \\ 0 & 0 & \partial\tilde{u}_z^{(a)}/\partial\tilde{y} \\ \partial\tilde{u}_x^{(a)}/\partial\tilde{y} & \partial\tilde{u}_z^{(a)}/\partial\tilde{y} & 0 \end{pmatrix},$$

$$\mathscr{A}_2 = \begin{pmatrix} 2\partial\tilde{u}_x^{(a)}/\partial\tilde{x} & \partial\tilde{u}_x^{(a)}/\partial\tilde{z} + \partial\tilde{u}_z^{(a)}/\partial\tilde{x} & 0 \\ \partial\tilde{u}_x^{(a)}/\partial\tilde{z} + \partial\tilde{u}_z^{(a)}/\partial\tilde{x} & 2\partial\tilde{u}_z^{(a)}/\partial\tilde{z} & 0 \\ 0 & 0 & 2\partial\tilde{u}_y^{(a)}/\partial\tilde{y} \end{pmatrix},$$

$$\mathscr{A}_3 = \begin{pmatrix} 0 & 0 & \partial\tilde{u}_y^{(a)}/\partial\tilde{x} \\ 0 & 0 & \partial\tilde{u}_y^{(a)}/\partial\tilde{z} \\ \partial\tilde{u}_y^{(a)}/\partial\tilde{x} & \partial\tilde{u}_y^{(a)}/\partial\tilde{z} & 0 \end{pmatrix}.$$

By algebra,

$$\boldsymbol{\Pi}^{*(a)}\langle \boldsymbol{n} \rangle = P_{sc}^* \left[\{0, 0, -\tilde{p}^{(a)}\} + \delta_a \left\{ \tilde{p}^{(a)} \frac{\partial\tilde{\eta}}{\partial\tilde{x}} + \frac{\partial\tilde{u}_x^{(a)}}{\partial\tilde{y}}, \tilde{p}^{(a)} \frac{\partial\tilde{\eta}}{\partial\tilde{z}} + \frac{\partial\tilde{u}_z^{(a)}}{\partial\tilde{y}}, 0 \right\} + O\left(\delta_a^2\right) \right]. \tag{A34}$$

In the liquid we find

$$\begin{aligned} \boldsymbol{\Pi}^{*(\ell)} = P_{sc}^* \Bigg[& -\tilde{p}^{(\ell)} \begin{pmatrix} 1 & 0 & 0 \\ 0 & 1 & 0 \\ 0 & 0 & 1 \end{pmatrix} + \frac{1}{Re_\ell \lambda} \begin{pmatrix} 0 & 0 & \partial\bar{u}_x^{(\ell)}/\partial\bar{y} \\ 0 & 0 & \partial\bar{u}_z^{(\ell)}/\partial\bar{y} \\ \partial\bar{u}_x^{(\ell)}/\partial\bar{y} & \partial\bar{u}_z^{(\ell)}/\partial\bar{y} & 0 \end{pmatrix} \\ & + \frac{1}{Re_\ell} \begin{pmatrix} 2\partial\bar{u}_x^{(\ell)}/\partial\tilde{x} & \partial\bar{u}_x^{(\ell)}/\partial\tilde{z} + \partial\bar{u}_z^{(\ell)}/\partial\tilde{x} & 0 \\ \partial\bar{u}_x^{(\ell)}/\partial\tilde{z} + \partial\bar{u}_z^{(\ell)}/\partial\tilde{x} & 2\partial\bar{u}_z^{(\ell)}/\partial\tilde{z} & 0 \\ 0 & 0 & 2\partial\tilde{u}_y^{(\ell)}/\partial\bar{y} \end{pmatrix} \\ & + \frac{\lambda}{Re_\ell} \begin{pmatrix} 0 & 0 & \partial\tilde{u}_y^{(\ell)}/\partial\tilde{x} \\ 0 & 0 & \partial\tilde{u}_y^{(\ell)}/\partial\tilde{z} \\ \partial\tilde{u}_y^{(\ell)}/\partial\tilde{x} & \partial\tilde{u}_y^{(\ell)}/\partial\tilde{z} & 0 \end{pmatrix} \Bigg]. \end{aligned} \tag{A35}$$

It is important to notice that the second matrix in (A35) is zero at leading order, in view of (A26). Therefore

$$\boldsymbol{\Pi}^{*(\ell)}\langle \boldsymbol{n}\rangle = P^*_{sc}\left[\left\{0,0,-\tilde{p}^{(\ell)}+\frac{2}{Re_\ell}\frac{\partial \tilde{u}_y^{(\ell)}}{\partial \bar{y}}\right\}+\delta_a\left\{\tilde{p}^{(\ell)}\frac{\partial \tilde{\eta}}{\partial \tilde{x}},\,\tilde{p}^{(\ell)}\frac{\partial \tilde{\eta}}{\partial \tilde{z}},0\right\}\right.$$
$$\left.+O\left(\frac{\delta_a}{Re_\ell}\right)+O\left(\frac{\lambda}{Re_\ell}\right)\right]. \tag{A36}$$

Equations (A31), (A34) and (A36) provide at leading order the conditions

$$\tilde{p}^{(\ell)}=\tilde{p}^{(a)},\quad \frac{\partial \tilde{u}_x^{(a)}}{\partial \tilde{y}}=0,\quad \frac{\partial \tilde{u}_z^{(a)}}{\partial \tilde{y}}=0 \tag{A37}$$

along the air–water interface. The first interfacial condition in (A37) and equation (A30) show that

$$\tilde{p}^{(\ell)}(\tilde{x},\tilde{y},\tilde{t})=\tilde{p}^{(a)}(\tilde{x},\tilde{y},\tilde{t})=:P(\tilde{x},\tilde{y},\tilde{t}).$$

We introduce the non-dimensional effective thickness of the air gap as

$$F(\tilde{x},\tilde{z},\tilde{t})=f(\tilde{x},\tilde{z})-\tilde{t}-\tilde{\eta}(\tilde{x},\tilde{z},\tilde{t})$$

and rewrite (A30) in the form

$$\frac{\partial^2 P}{\partial \tilde{x}^2}+\frac{\partial^2 P}{\partial \tilde{z}^2}+\frac{\partial^2 F}{\partial \tilde{t}^2}=0, \tag{A38}$$

which connects the pressure in the air gap $P(\tilde{x},\tilde{z},\tilde{t})$ and the effective thickness of this gap $F(\tilde{x},\tilde{z},\tilde{t})$. In the two-dimensional case (A38) takes the form

$$\frac{\partial^2 P}{\partial \tilde{z}^2}+\frac{\partial^2 F}{\partial \tilde{t}^2}=0, \tag{A39}$$

which should be integrated under the symmetry condition $\partial P/\partial \tilde{z}(0,\tilde{t})=0$ and the condition at infinity $P(\tilde{z},\tilde{t})\to 0$, as $|\tilde{z}|\to\infty$.

Conditions (A13) and (A37) are used to integrate (A12). First we integrate (A12c) with respect to $\tilde{y}$ across the air gap thickness. The result is exact in the model with incompressible air,

$$\frac{\partial}{\partial \tilde{x}}\int_{\tilde{\eta}(\tilde{x},\tilde{z},\tilde{t})}^{f(\tilde{x},\tilde{z})-\tilde{t}}\tilde{u}_x^{(a)}(\tilde{x},\tilde{z},\tilde{y},\tilde{t})\,\mathrm{d}\tilde{y}+\frac{\partial}{\partial \tilde{z}}\int_{\tilde{\eta}(\tilde{x},\tilde{z},\tilde{t})}^{f(\tilde{x},\tilde{z})-\tilde{t}}\tilde{u}_z^{(a)}(\tilde{x},\tilde{z},\tilde{y},\tilde{t})\,\mathrm{d}\tilde{y}=-\frac{\partial F}{\partial \tilde{t}}. \tag{A40}$$

Conditions (A13), (A37) and equations (A12a,b) then provide

$$\int_{\tilde{\eta}(\tilde{x},\tilde{z},\tilde{t})}^{f(\tilde{x},\tilde{z})-\tilde{t}}\tilde{u}_x^{(a)}(\tilde{x},\tilde{z},\tilde{y},\tilde{t})\mathrm{d}\tilde{y}=-\frac{1}{3}\frac{\partial P}{\partial \tilde{x}}F^3(\tilde{x},\tilde{z},\tilde{t}),$$

$$\int_{\tilde{\eta}(\tilde{x},\tilde{z},\tilde{t})}^{f(\tilde{x},\tilde{z})-\tilde{t}}\tilde{u}_z^{(a)}(\tilde{x},\tilde{z},\tilde{y},\tilde{t})\mathrm{d}\tilde{y}=-\frac{1}{3}\frac{\partial P}{\partial \tilde{z}}F^3(\tilde{x},\tilde{z},\tilde{t}).$$

Hence (A40) takes the form

$$\mathrm{div}[F^3\nabla P]=3F_{\tilde{t}} \tag{A41}$$

which in the two-dimensional case is

$$\frac{\partial}{\partial \tilde{z}}\left[F^3\frac{\partial P}{\partial \tilde{z}}\right]=3\frac{\partial F}{\partial \tilde{t}}. \tag{A42}$$

In the main body of this paper we restrict ourselves to the two-dimensional case, with (A39) and (A42) representing the nonlinear model of strong air–water interaction, giving (2.5), (2.6) respectively.

A.7. *Further checks and comments*

The asymptotic analysis so far has neglected compressibility effects in the air. However, we can conclude that the air compressibility (as well as liquid compressibility) can be neglected when the pressure scale P^*_{sc} defined by (A18) is much smaller than the product $\rho^*_a c^{*2}_a$, recalling that c^*_a is the speed of sound in air at rest. This gives

$$\frac{V^{*2}}{c^{*2}_a} \ll Re_a \delta^4_a = \frac{\epsilon H^*_b}{R^*_x}.$$

Taking account of the compressibility restriction, the inequality (A25) has to be modified to

$$\max\left\{\frac{M^2_a}{\epsilon}, \frac{\epsilon}{Re_a æ^{2/3}}\right\} \ll \frac{H^*_b}{R^*_x} \ll \left(\frac{\epsilon}{Re_a}\right)^{1/3}, \tag{A43}$$

where $M_a = V^*/c^*_a$ is the Mach number. Such a range of ratios H^*_b/R^*_x exists if and only if $V^* R^*_x \gg \nu_\ell$, as was shown earlier, and $M^2_a \epsilon^{-1} \ll \epsilon^{1/3} Re^{-1/3}_a$. By using definitions of M_a, ϵ and Re_a, the latter inequality can be presented as

$$V^7 R^*_x \ll \epsilon^4 \nu^*_a c^{*6}_a, \tag{A44}$$

where $\epsilon^4 \nu^*_a c^{*6}_a \approx 0.047\,\mathrm{m^8\,s^{-7}}$. Therefore the air compressibility can be of importance even for the moderate speeds of the body.

In the analysis we have assumed so far that the aerodynamic pressure $p^{*(a)}$ in the air gap is equal to the hydrodynamic pressure $p^{*(\ell)}$ in the liquid layer on the air–water interface. This means the surface tension could be neglected in our analysis. For small bodies the curvature of the interface is scaled as $\kappa^* = \tilde{\kappa}/R^*_x$, where $\tilde{\kappa}$ is the non-dimensional curvature. The surface tension contribution to the dynamic boundary condition at the air–water interface can be neglected if $\sigma^* \kappa^*/p^{*(a)} \ll 1$, where σ^* is the coefficient of surface tension. This inequality yields

$$\frac{1}{R^*_x} \frac{\sigma^* \tilde{\kappa}}{P^*_{sc} \tilde{p}^{(a)}} \ll 1, \tag{A45}$$

where the pressure scale P^*_{sc} is given by (A18). Inequality (A45) will be used in the following in the form

$$\frac{\tilde{\kappa}}{\tilde{p}^{(a)}} \ll f, \qquad f = \frac{R^*_x P^*_{sc}}{\sigma^*}, \tag{A46}$$

where $\tilde{p}^{(a)}$ is the non-dimensional pressure in the air gap.

The analysis of § 5 indicates that the curvature of the air–water interface becomes very large near touchdown, where the interface approaches the body surface at a high speed. Therefore this analysis can be used only until just before the touchdown instant, and the surface tension (among other new physical features) must be taken into account, where the curvature is large. The limit in time of the present analysis is provided by (A46), with the non-dimensional parameter f being of major importance. This parameter is calculated by using (A18) and the definition of δ_a for the shallow layer case as

$$f = \frac{V^{*2} R^{*2}_x \rho^*_\ell}{\sigma^* H^*_b}. \tag{A47}$$

For the air–water interface, $\sigma^* = 7.25 \times 10^{-2}$ N/m. If $R_x^* = 5$ mm and $V^* = 1$ m/s, then $Re_a^{-1} \approx 2.6 \times 10^{-3}$ and $\epsilon/Re_a \approx 2.6 \times 10^{-6}$. In this case the liquid layer can be treated as shallow during the touchdown stage if $H_b^* < 5 \times 10^{-5}$ m. Taking $H_b^* = 10^{-5}$ m, we obtain from (A47) that $f \approx 3400$. This numerical value and the inequality (A46) applied to the solution studied in this paper provide the time interval before touchdown during which the contribution of the surface tension can be neglected.

REFERENCES

Afandizadeh Zargari, E., Jimack, P. K. & Walkley, M. A. 2007 An investigation of the film thickness calculation for elastohydrodynamic lubrication problems.In *Proc. 9th Conf. on Numerical Methods for Fluid Dynamics*. ICFD, Reading.

Brocchini, M. & Peregrine, D. H. 1996 Integral flow properties of the swash zone and averaging. *J. Fluid Mech.* **317**, 241–273.

Couder, Y., Fort, E., Gautier, C. H. & Boudaoud, A. 2005*a* From bouncing to floating drops: Non-coalescence of drops in a fluid bath. *Phys. Rev. Lett.* **94**, 177801.

Couder, Y., Protiere, S., Fort, E. & Boudaoud, A. 2005*b* Dynamical phenomena: Walking and orbiting droplets. *Nature* **437**, 208.

Gent, R. W., Dart, N. P. & Cansdale, J. T. 2000 Aircraft icing. *Phil. Trans. R. Soc. Lond.* A **358**, 2873–2911.

Howison, S. D., Ockendon, J. R. & Oliver, J. M. 2002 Deep- and shallow-water slamming at small and zero deadrise angles. *J. Engng Maths* **42**, 373–388.

Howison, S. D., Ockendon, J. R., Oliver, J. M., Purvis, R. & Smith, F. T. 2005 Droplet impact on a thin fluid layer. *J. Fluid Mech.* **542**, 1–25.

Howison, S. D., Ockendon, J. R. & Wilson, S. K. 1991 Incompressible water entry problems at small deadrise angles. *J. Fluid Mech.* **222**, 215–230.

Josserand, C. & Zaleski, S. 2003 Droplet splashing on a thin liquid film. *Phys. Fluids* **15**, 1650–1657.

Korobkin, A. A. 1996 Water impact problems in ship hydrodynamics. In *Advances in Marine Hydrodynamics* (ed. M. Ohkusu),pp. 323–371. Computational Mechanics Publications, Southampton.

Korobkin, A. A. 1997 Asymptotic theory of liquid–solid impact. *Phil. Trans. R. Soc. Lond.* A **355**, 507–522.

Korobkin, A. A. 1999 Shallow water impact problems. *J. Engng Maths* **35**, 233–250.

Korobkin, A. A. 2006 Two-dimensional problem of the impact of a vertical wall on a layer of a partially aerated liquid. *J. Appl. Mech. Tech. Phys.* **47**, 643–653.

Korobkin, A. A. & Khabakhpasheva, T. I. 1997 A shallow solid body approaching the interface of two media. *J. Appl. Mech. Tech. Phys.* **38**, 857–867.

Korobkin, A. A. & Khabakhpasheva, T. I. 2006 Impact on the boundary of a compressible two-layer fluid. *Fluid Dyn.* **41**, 263–277.

Liow, J. L. 2001 Splash formation by spherical drops. *J. Fluid Mech.* **427**, 73–105.

Oliver, J. M. 2002 Water entry and related problems. PhD thesis, University of Oxford.

Pan, K. L. & Law, C. K. 2007 Dynamics of droplet-film collision. *J. Fluid Mech.* **587**, 1–22.

Protiere, S., Boudaoud, A. & Couder, A. 2006 Particle-wave association on a fluid interface. *J. Fluid Mech.* **554**, 85–108.

Purvis, R. & Smith, F. T. 2004*a* Large droplet impact on water layers.*AIAA Paper* 2004–0414.

Purvis, R. & Smith, F. T. 2004*b* Air–water interactions near droplet impact. *Eur. J. Appl. Maths* **15**, 853–871.

Purvis, R. & Smith, F. T. 2005*a* Droplet impact on water layers: Post-impact analysis and computations. *Phil. Trans. R. Soc. Lond.* A **363**, 1209–1221.

Purvis, R. & Smith, F. T. 2005*b* Air effects on droplet impact. *AIAA Paper* 2005-5184.

Quero, M., Hammond, D. W., Purvis, R. & Smith, F. T. 2006 Analysis of super-cooled water droplet impact on a thin water layer and ice growth.*AIAA Paper* 2006-466.

Smith, F. T. 1982 On the high Reynolds number theory of laminar flows. *IMA J. Appl. Maths* **28**, 207–281.

Smith, F. T. 1988 Finite-time break-up can occur in any unsteady interactive boundary layer. *Mathematika* **35**, 256–273.

Smith, F. T., Li, L. & Wu, G.-X. 2003 Air cushioning with a lubrication/inviscid balance. *J. Fluid Mech.* **482**, 291–318.

Sobey, I. 2000 *Introduction to Interactive Boundary Layer Theory*. Oxford University Press.

Tan, C. S. & Papadakis, M. 2005 Droplet breakup, splashing and re-impingement on an iced airfoil. In *4th AIAA Theoretical Fluid Mechanics Meeting*.

Thorodssen, S. T. 2002 The ejecta sheet generated by the impact of a drop. *J. Fluid Mech.* **451**, 373–381.

Vanden-Broeck, J.-M. 2001 Damped waves generated by a moving pressure distribution. *Eur. J. Appl. Maths* **12**, 357–366.

Vanden-Broeck, J.-M. & Miloh, T. 1996 The influence of a layer of mud on the train of waves generated by a moving pressure distribution. *J. Engng Maths* **30**, 387–400.

Wilson, S. K. 1991 A mathematical model for the initial stages of fluid impact in the presence of a cushioning fluid layer. *J. Engng Maths* **25**, 265–285.